

Supporting information

Production of Highly Monolayer Enriched Dispersions of Liquid-Exfoliated Nanosheets by Liquid Cascade Centrifugation

Claudia Backes,^{1,2} Beata M. Szydłowska,^{1,2} Andrew Harvey,^{1,2} Shengjun Yuan,³ Victor Vega-Mayoral,^{4,5} Ben R. Davies,^{1,2} Pei-liang Zhao,⁶ Damien Hanlon,^{1,2} Elton J. G. Santos,⁷ Mikhail I. Katsnelson,³ Werner J Blau,^{1,2} Christoph Gadermaier,^{4,5} and Jonathan N. Coleman^{1,2*}

¹*CRANN & AMBER, Trinity College Dublin, Dublin 2, Ireland*

²*School of Physics, Trinity College Dublin, Dublin 2, Ireland*

³*Institute for Molecules and Materials, Radboud University of Nijmegen, Heijendaalseweg 135, 6525AJ Nijmegen, the Netherlands*

⁴*Department for Complex Matter, Jozef Stefan Institute, Jamova 39, 1000 Ljubljana, Slovenia*

⁵*Jozef Stefan International Postgraduate School, Jamova 39, 1000 Ljubljana, Slovenia*

⁶*Department of Applied Physics, Zernike Institute for Advanced Materials, University of Groningen, Nijenborgh 4, NL-9747AG Groningen, The Netherlands*

⁷*School of Mathematics and Physics and School of Chemistry and Chemical Engineering, Queen's University Belfast, Stranmillis Road, Room 0G.423, Belfast, BT95AL, United Kingdom*

*colemaj@tcd.ie

Contents

0	Methods.....	3
1	Basic characterization of LCC size-selected WS ₂	9
1.1	Transmission electron microscopy (TEM)	9
1.2	Atomic force microscopy (AFM)	12
1.3	Extinction coefficient and produced masses	19
2	UV-Vis <L> and <N> metric.....	21
2.1	Alternative L metrics	21
2.2	Second derivatives of extinction spectra to obtain <N>.....	22
2.3	Optical characterization of very small nanosheets discarded in the primary cascade	23

3	Further examples of fitted PL spectra.....	24
4	Robustness of metrics towards stabilizer concentration.....	26
5	Comparison different centrifugation procedures.....	28
6	Monolayer enrichment.....	36
6.1	General centrifugation procedure.....	36
6.2	Example scenario 1: Spectroscopic data and AFM.....	37
6.3	Example scenario 2: Spectroscopic data and AFM.....	40
6.4	Further optical characterization of ML-rich samples and edge effects.....	43
6.5	Example scenario 3.....	47
6.6	Example Scenario 4.....	49
7	Fitting of the second derivatives of the A-exciton: methodology and examples of standard size-selected samples.....	51
8	Supporting References.....	55

0 Methods

Sample preparation:

WS₂ dispersions were prepared by probe sonicating the powder (Sigma Aldrich, initial concentration 20 g/L) in an aqueous surfactant solution (typically sodium cholate SC; sodium dodecyl sulfonate SDBS or poly(vinyl alcohol) PVA to a minor extent). WS₂ was immersed in 80 mL of aqueous surfactant solution ($C_{\text{surf}} = 6\text{g/L}$). The mixture was sonicated under ice-cooling in a 100 mL metal beaker by probe sonication using a solid flathead tip (Sonics VX-750) for 1 h at 60 % amplitude with a pulse of 6 s on and 2 s off. The dispersion was centrifuged in 15 mL aliquots using 28 mL vials in a Hettich Mikro 220R centrifuge equipped with a fixed-angle rotor 1016 at 5 krpm (2660 g) for 1.5 h. The supernatant was discarded and the sediment collected in 80 mL of fresh surfactant ($C_{\text{SC}} = 2\text{g/L}$) and subjected to a second sonication using a solid flathead tip (Sonics VX-750) for 5 h at 60 % amplitude with a pulse of 6 s on and 2 s off. From our experience, this two-step sonication procedure yields a higher concentration of exfoliated WS₂ and removes impurities.

To select nanosheets by size, we used liquid cascade centrifugation (Hettich Mikro 220R centrifuge, 15 °C) with sequentially increasing rotation speeds. Two different rotors were used. For speeds ≤ 5 krpm, a fixed angle rotor 1016 was used (28 mL vials, ~ 10 mL aliquots in each vial). For this centrifuge and this rotor, the centrifugation rate, f is related to the centrifugal force *via* $RCF = 106.4 f^2$ where f is the rotation rate in krpm. For speeds > 5 krpm, samples were centrifuged in a 1195-A fixed angle rotor (1.5 mL vials), where f is related to the centrifugal force *via* $RCF = 97.4 f^2$. The following procedure was applied as standard size selection of the primary cascade: Unexfoliated WS₂ was removed by centrifugation at 1.5 krpm (240 g, 2 h). The supernatant was subjected to further centrifugation at 2 krpm (426 g, 2 h). The sediment was collected in fresh surfactant at reduced volume (3-8 mL), while the supernatant was centrifuged at 3 krpm (958 g, 2 h). Again, the sediment was collected and the supernatant subjected to centrifugation at higher speeds. This procedure was repeated with the following speeds: 4 krpm (1700 g, 2 h), 5 krpm (2660 g, 2 h), 6 krpm (3506 g, 2 h), 7.5 krpm (5480 g, 2 h), 10 krpm (9740 g, 2 h). The data presented in Figure 1 uses the central rpm/g-force to express the consecutive centrifugation. For example, the sediment collected from the centrifugation between 2-3 krpm has a central rpm of 2.5 krpm (665 g).

To demonstrate the broader applicability of the size selection procedure, a similar primary cascade was used in solvent rather than aqueous surfactant solution. For this purpose, WS₂ was exfoliated under equal sonication conditions (including the sediment recycling step) in *N*-methyl-2-pyrrolidone rather than water-SC. The stock dispersion was centrifuged (2h each) with the following rpms: 1 krpm and sediment discarded, supernatant subjected to 1.5 krpm (sediment 1-1.5 krpm collected), supernatant after this step centrifuged at 2 krpm (sediment 1.5-2krpm collected), followed by 2.5 krpm (to collect 2-2.5 krpm), 3 krpm (2.5-3 krpm), 5 krpm (3-5 krpm) and finally 10 krpm (5-10 krpm). The thus produced WS₂ collected in the sediments were redispersed to yield WS₂ concentrations of ~ 1 g/L and subjected to extinction spectroscopy. To facilitate the measurement of liquid Raman/PL and to test for solvatochromic shifts in the length and thickness metric, the samples were transferred to water-SC (SC concentration 2 g/L) by high speed centrifugation at 31,600 g. The sediments were redispersed by mild sonication (5 min bath) in water-SC, centrifuged again at 31,600 g to remove traces of NMP in the supernatant to yield WS₂-SC dispersion that were produced from originally exfoliating in NMP.

To perform the monolayer enrichment, a sample size-selected by the standard procedure was subjected to further iterative centrifugation steps. Details are described in Section 4 of the Supplementary Information. The sample of S.C.1 shown in Figure 6 was produced from a standard size selection between 6-8 krpm (volume reduced to 3 mL, all further centrifugation performed in fixed angle rotor 1195-A). The dispersion was centrifuged at 4 krpm (1560 g) for 6 h. the sediment was discarded and the supernatant centrifuged at 5 krpm (2435 g) for 14 h. The sediment was discarded and the supernatant centrifuged at 9 krpm (7890 g, 4 h). The supernatant contained very small nanosheets, which showed significantly reduced photoluminescence (see SI section 4). The sediment was collected and centrifuged again at 15 krpm (21915 g, 1 h) to further remove very small nanosheets. The sediment after this centrifugation was collected and had a monolayer volume fraction of > 60%. Alternatively, for S.C.2 a stock dispersion where only unexfoliated (1.5 krpm, 240 g, 2 h) and very small nanosheets (10 krpm, 9740 g, 2 h) were removed was used as starting point for the secondary cascade. The volume after the 10 krpm centrifugation was reduced to 4.5 mL. The dispersion was centrifuged as follows: 2.5 krpm (609 g, 16 h), supernatant subjected to 4 krpm (1560 g, 14 h), supernatant subjected to 10 krpm (9740 g, 1 h), sediment collected in 1.5 mL and subjected to 5 krpm (2436 g, 5 h), supernatant subjected to 8 krpm (6235 g, 2 h), sediment collected and subjected to 3 krpm (877 g, 12 h). The supernatant after this last centrifugation step was collected and had a monolayer volume fraction of ~70-75%.

Characterization:

Optical extinction was measured on a Varian Cary 500 in quartz cuvettes with a pathlength of 0.4 cm typically in 1 nm increments.

Bright field transmission electron microscopy imaging was performed using a JEOL 2100, operated at 200 kV. Holey carbon grids (400 mesh) were purchased from Agar Scientific and prepared by diluting dispersion to a low concentration (typical optical densities at C-exciton of 0.3-0.5) and drop casting onto a grid placed on a filter membrane to wick away excess solvent. Statistical analysis was performed of the flake dimensions by measuring the longest axis of the nanosheet and assigning it “length” and the dimension perpendicular to it and assigning it as “width”.

Atomic force microscopy (AFM) was carried out on a VeecoNanoscope-IIIa (Digital Instruments) system equipped with a E-head (13 μm scanner) in tapping mode after depositing a drop of the dispersion (10 μL) on a pre-heated (150 $^{\circ}\text{C}$) Si/SiO₂ wafer with an oxide layer of 300 nm. The high concentration dispersions collected after LCC were diluted with water (to optical densities at C-exciton of 0.1-0.2) immediately prior to deposition to reduce surfactant concentrations. After deposition, the wafer was rinsed with ~ 5 mL of water and ~ 5 mL of isopropanol. Typical image sizes ranged from $1 \times 1 \mu\text{m}^2$ to maximum $4 \times 4 \mu\text{m}^2$ for the larger nanosheets at scan rates of 0.4-0.6 Hz with 512 lines per image. The apparent thickness was converted to number of layers using previously elaborated step-height analysis of liquid-exfoliated nanosheets.¹

Raman and photoluminescence spectroscopy was performed on the liquid dispersions using a Horiba Jobin Yvon LabRAM HR800 with 532 nm excitation laser in air under ambient conditions. The Raman/PL emission was collected by 100 \times objective lens (N.A. = 0.8) and dispersed by 600 gr/mm with 10 % of the laser power (~ 2 mW). Great care must be taken during these measurements, as changes in the focal plane during the acquisition will introduce an error in the PL/Raman ratio. This is often reflected in a tilted baseline or asymmetric PL due to innerfilter and reabsorption effects. It can also be visually recognized when the size of the laser spot in the optical image has changed during the measurement. The following procedure was used to ensure reproducibility: A drop ($\sim 40 \mu\text{L}$) of a high concentration dispersion (optical densities at C-exciton > 3) was placed on a glass slide and the drop edge was optically focused using a 10 \times objective. The focus for the measurement

with the 100× objective was readjusted in such a way that the laser was focused slightly above the drop. Focusing inside the drop leads to innerfilter and reabsorption effects causing the WS₂ PL to be asymmetric and lower in intensity. We also note that measurements taken close to the drop edge were more reliable than in the center of the drop because the focus remained constant throughout the measurement due to the lower curvature of the drop and hence negligible changes in the focus by evaporation of water. The average of ~5 measurements are displayed. Acquisition times were kept as short as possible depending on the concentration of the dispersion (between 2-10 s per frame).

Photoluminescence to obtain the contour plot and excitation spectra was measured in quartz cuvettes using an Edinburgh Instruments FS920 PL spectrometer equipped with a Xe lamp (450 W) and a S900 photomultiplier tube detector at room temperature with single monochromators in excitation and emission. Typical bandwidths were 3-5 nm with acquisition times of 0.3-0.5s. To avoid artifacts from scattering of the nanomaterial dispersion, a 550 nm cut-off filter was placed on the emission side. The excitation was corrected for the light intensity.

Theoretical Optical Gap Calculations:

The optical gap is extracted from the optical conductivity calculated by using the tight-binding propagation method (TBPM).^{2,3} We adopt an 11-band TB model of few-layered WS₂ proposed by R. Roldán *et al* in Ref.⁴, consisting with five d orbitals of W atom and six p orbitals of S atom as the follows:

$$\text{W atoms: } d_{3z^2-r^2}, d_{x^2-y^2}, d_{xy}, d_{xz}, d_{yz},$$

$$\text{S atoms: } p_{x,t}, p_{y,t}, p_{z,t}, p_{x,b}, p_{y,b}, p_{z,b},$$

where the *t* and *b* indexes indicate the top and bottom planes of S atoms within the same layer, respectively. The Slater-Koster parameters used to construct the intralayer W-S, W-W and S-S hopping matrixes are (in unit of eV) $\Delta_0 = -0.872$, $\Delta_1 = 0.42$, $\Delta_2 = -2.065$, $\Delta_p = -3.468$, $\Delta_z = -3.913$, $V_{pd\sigma} = 3.603$, $V_{pd\pi} = -0.942$, $V_{dd\sigma} = -1.216$, $V_{dd\pi} = 0.177$, $V_{dd\delta} = 0.243$, $V_{pp\sigma} = 0.749$, $V_{pp\pi} = 0.236$, and for the interlayer S-S hoppings are $U_{pp\sigma} = -0.55$, $U_{pp\pi} = -0.6$. The spin-orbital couplings originating from the W and S atoms are $\lambda_W = 0.215$, $\lambda_S = 0.057$.

The real part of the optical conductivity at finite frequency is calculated *via* the Kubo's formula as²⁻⁴

$$\sigma(\omega) = \lim_{\varepsilon \rightarrow +0} \frac{1 - e^{-\beta\hbar\omega}}{\hbar\omega\Omega} \int_0^{\infty} dt e^{i(\omega+i\varepsilon)\tau} 2i \text{Im} \langle \phi | J[1 - f(H)]J(\tau)f(H) | \phi \rangle,$$

where Ω is the sample area, $\beta = 1/k_B T$ is the inverse temperature, H is the tight-binding Hamiltonian, $f(H) = 1/\{\exp[\beta(H - \mu)] + 1\}$ is the Fermi-Dirac distribution operator, and $J(\tau) = \exp(iH\tau/\hbar)J\exp(-iH\tau/\hbar)$ is the current operator in the Heisenberg picture. The state $|\phi\rangle$ is a normalized random state which covers all the eigenstates in the whole spectrum.² The time evolution operator and Fermi-Dirac distribution operator are represented as the Chebyshev polynomial expansions.

The numerical method implemented here has the advantage that the CPU time and the memory costs are both linear dependent on the sample size, and the presented results are obtained from samples consisting of $\sim 6 \times 10^6$ atomic sites ($\sim 2 \times 10^7$ atomic orbitals).

Ab initio GW-BSE simulations:

We start the optical calculations using the Kohn-Sham eigenvectors and energy eigenvalues previously calculated within the density-functional theory at generalized-gradient approximation⁵, for monolayer and bilayer WS₂, using plane waves basis set and periodic boundary conditions as implemented in the PWscf⁶ and Vasp^{7,8} codes. Norm-conserving⁹ and PAW^{10,11} pseudopotentials are used with a plane wave energy cutoff of 900 eV, with partial-core states included. Atomic coordinates were allowed to relax until all forces were smaller in magnitude than 0.01 eV/Å. Relevant lattice constants (in-plane and out-of-plane) were optimized for each system. To avoid interactions between supercell images, the distance between periodic images of the WS₂ layers along the direction perpendicular to the plane was always larger than 20 Å. Spin-orbit interactions are included in the calculations perturbatively through the calculations of the spinor wave functions, which are used as an input for the calculation of the dielectric functions $\varepsilon_2(\omega, q)$ afterwards. The GW-BSE calculations are done using the Yambo code¹² using 300 unoccupied bands in the integration of the self-energy term. The number of k -points was chosen according to the Monkhorst–Pack scheme¹³ and was set to the equivalent of a $21 \times 21 \times 1$ grid in the primitive unit cell of WS₂, which was previously converged for all structures. The BSE Hamiltonian was created using the ten highest valence bands and the six lowest conduction bands using the Tamm-Dancoff approach. The response functions were obtained in a fine grid of 1000 energy points using a broadening of 0.04 eV in all calculations.

1 Basic characterization of LCC size-selected WS_2

1.1 Transmission electron microscopy (TEM)

Samples from standard LCC

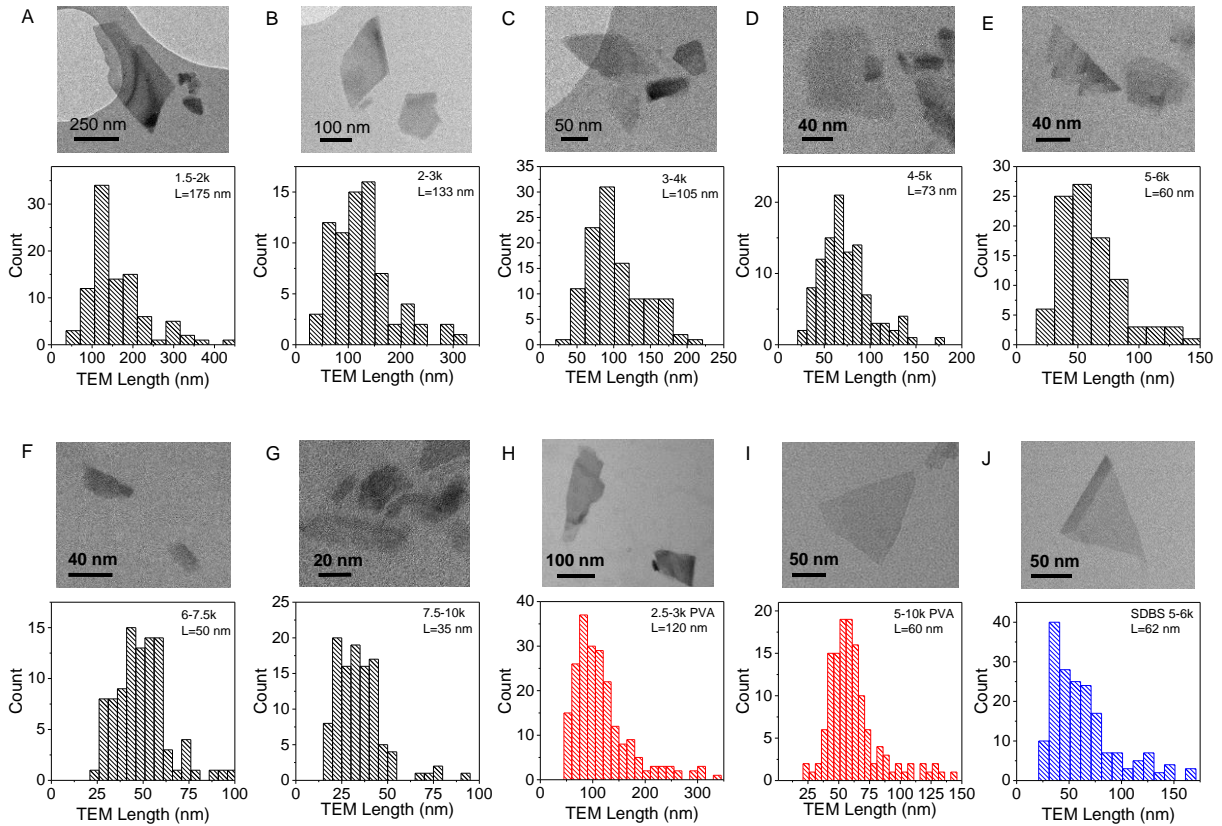


Figure S1: TEM images and length histograms of the WS_2 samples obtained from the standard LCC as described in the methods section. A-G) WS_2 dispersed in an aqueous solution of sodium cholate (SC, 2 g/L) after centrifugation between A) 1.5-2 krpm, B) 2-3 krpm, C) 3-4 krpm, D) 4-5 krpm, E) 5-6 krpm, F) 5-7.5 krpm, G) 7.5-10 krpm. H-I) WS_2 dispersed in an aqueous solution of poly(vinyl alcohol) (PVA, 2 g/L) after centrifugation between H) 2.5-3 krpm, I) 5-10 krpm. J) WS_2 dispersed in an aqueous solution of sodium dodecyl sulfonate (SDBS, 2 g/L) after centrifugation between 5-6 krpm.

Very small nanosheets removed in the final supernatant of the standard primary cascade

In our standard size selection cascade, we discard the very small nanosheets in the supernatant after 10 krpm. This is mostly because nanosheets are too small to allow for an accurate AFM analysis. However, it is nonetheless important to provide insights in their properties. To do this, we have added a centrifugation step at 15 krpm to collect most of these nanosheets and subjected the sample to TEM and optical characterization. While the TEM (figure S2) shows these are indeed small, but clearly 2D nanosheets with $\langle L \rangle = 25$ nm, their optical properties (see figure S13) are distinct which tempted us to set 10 krpm as upper boundary in the standard centrifugation cascade.

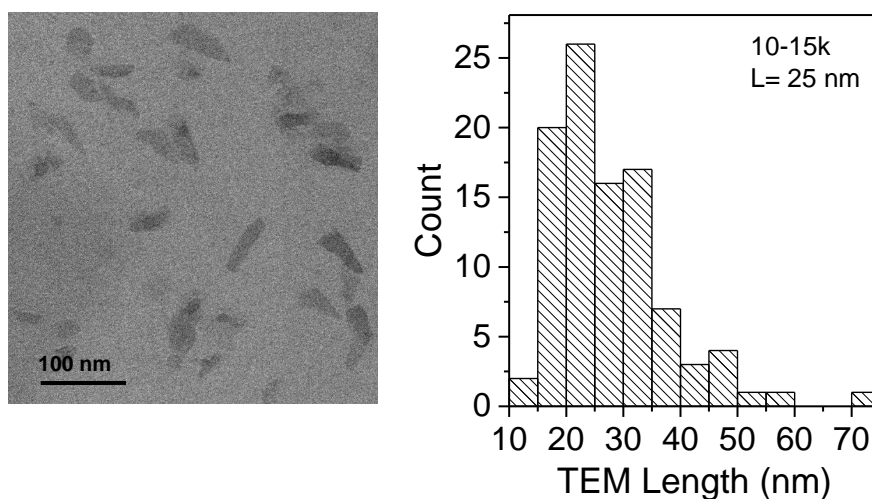


Figure S2: TEM analysis of the fraction of the smallest nanosheets discarded in the supernatant after centrifugation at 10 krpm in the standard cascade. To facilitate characterization, these were collected in the sediment after a centrifugation at 15 krpm. Left: TEM image showing that this material is indeed small, but clearly 2D nanosheets. Right: TEM length histogram yielding a mean length of 25 nm.

Large nanosheets produced by band sedimentation

To test whether the length metric based on intensity ratios in the extinction spectra also apply to larger nanosheets (which tend to be thicker), we have prepared a number of dispersion containing larger WS₂ nanosheets by band sedimentation as described previously for liquid exfoliated MoS₂¹ and subjected a subset of the samples to TEM (see Figure S3).

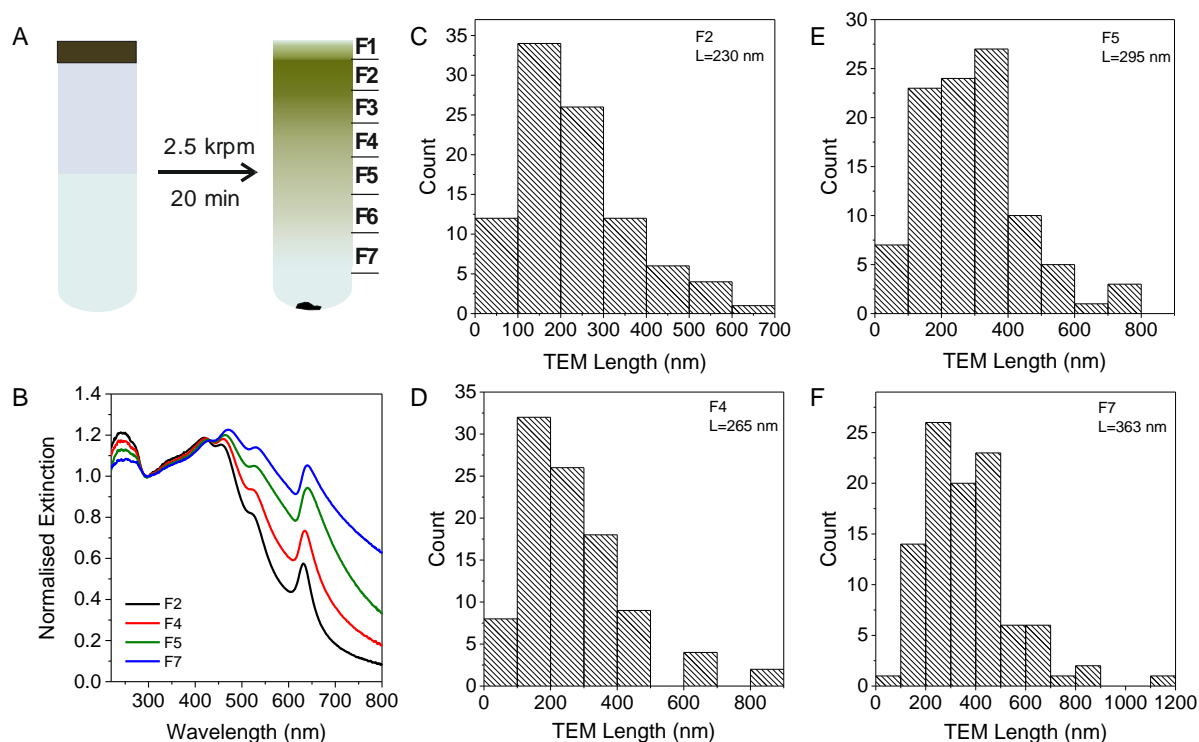


Figure S3: Production of larger WS₂ nanosheets by band sedimentation. A) Schematic representation of the band sedimentation procedure. Prior to band sedimentation, 1 mL of the stock dispersion of the nanomaterial in aqueous SC was layered on top of the race layer containing 5 mL of deuterated water at the bottom and 5 mL of 1-1 mixture of deuterated water in the middle. The surfactant concentration was kept constant throughout the vial. After centrifugation in a Heraeus Megafuge 16 benchtop centrifuge equipped with a 3655 swinging bucket rotor at 2.5 krpm (1175 g), 20 min, 8 fractions (F1-F8) were collected from the initial 11 mL liquid from top to bottom. Both layering and fractionation were performed by hand using Pasteur pipettes. F2, F4, F5 and F7 were subjected to further analysis. B) Normalized extinction spectra of the fractions F2, F4, F5 and F7. C-F) TEM length histograms of the fractions. C) F2, D) F4, E) F5, F) F7.

1.2 Atomic force microscopy (AFM)

Samples from standard LCC

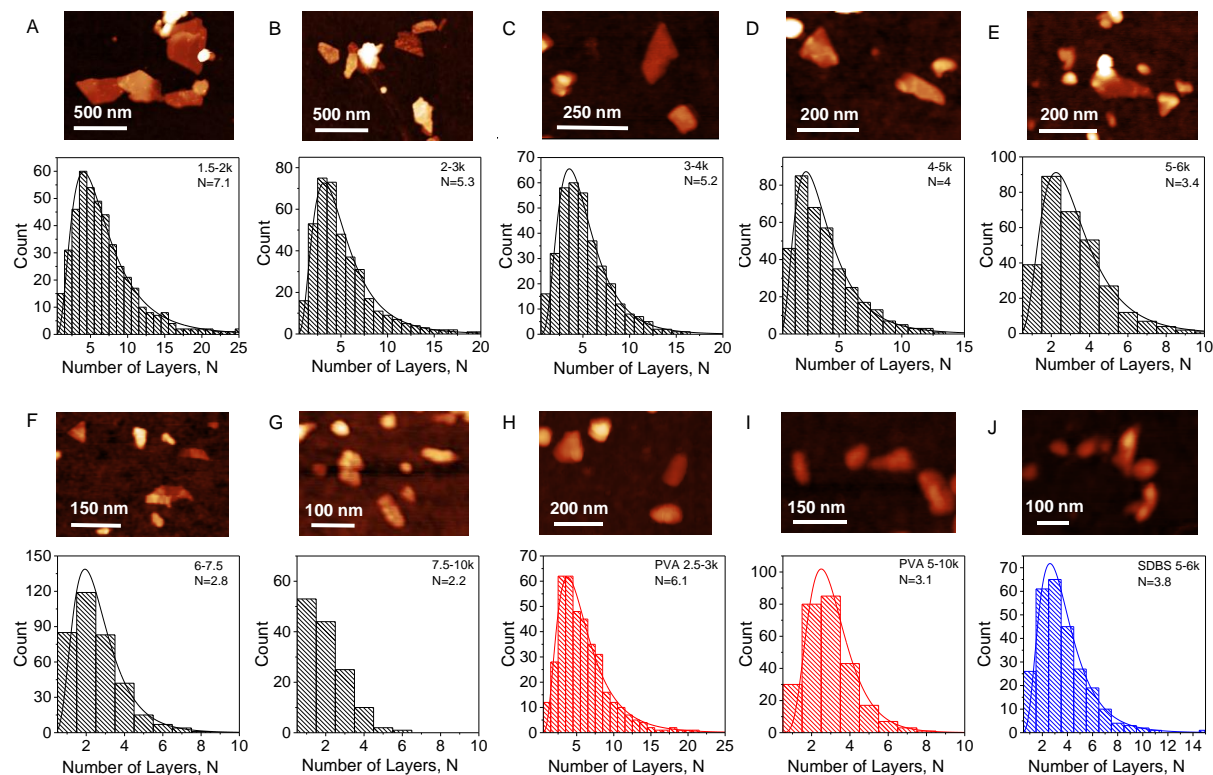


Figure S4: AFM images and number of layer histograms of the WS_2 samples obtained from the standard LCC as described in the methods section. A-G) WS_2 dispersed in an aqueous solution of sodium cholate (SC, 2 g/L) after centrifugation between A) 1.5-2 krpm, B) 2-3 krpm, C) 3-4 krpm, D) 4-5 krpm, E) 5-6 krpm, F) 5-7.5 krpm, G) 7.5-10 krpm. H-I) WS_2 dispersed in an aqueous solution of poly(vinyl alcohol) (PVA, 2 g/L) after centrifugation between H) 2.5-3 krpm, I) 5-10 krpm. J) WS_2 dispersed in an aqueous solution of sodium dodecyl benzenesulfonate (SDBS, 2 g/L) after centrifugation between 5-6 krpm. Notably all histograms are log-normal in shape as indicated by the solid line.

Step height analysis

Apparent AFM heights from liquid exfoliated nanomaterials are usually overestimated due to residual solvent.^{1, 14, 15} To overcome these problems and to convert the apparent measured AFM thickness to the number of layers, we have therefore applied a similar approach as reported for graphene, MoS₂, GaS and black phosphorus.^{1, 14, 16, 17} This involves measuring the height of steps associated with terraces of incompletely exfoliated nanosheets on the nanosheet surface as illustrated in a few cases in figure S5. In total, >60 height profiles such as the ones shown in figure S5 were examined and the step heights were plotted in ascending order in figure S6. The apparent height of each step is always a multiple of a discrete value which represents the apparent height of one WS₂ monolayer seen by the AFM even though the theoretical thickness is much smaller. The step height of one LPE WS₂ monolayer was determined as 1.9 nm. Hence, to convert the measured apparent AFM height to number of layers, the measured height was divided by 1.9 nm throughout this manuscript.

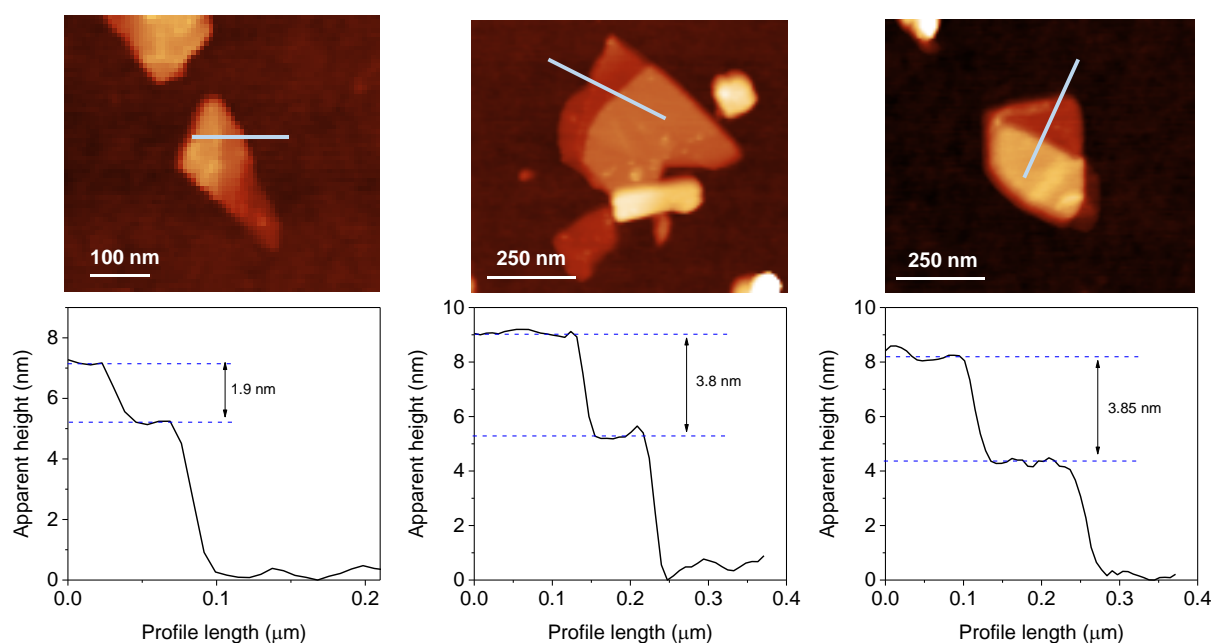


Figure S5: Height profiles across WS₂ nanosheets with steps. The profile was taken along the lines shown on the corresponding nanosheets. The dashed blue lines indicate where the heights for the step height analysis were taken. The related step heights in nm are also shown. The error in assessing the height profile is ~ 0.3 nm.

Currently, it is unclear why the apparent height of liquid exfoliated nanosheets is overestimated in AFM. However, we note that we have also observed this for LPE graphene,¹⁴ MoS₂,¹ GaS¹⁶ and black phosphorus.¹⁷ In the case of graphene and MoS₂, we were able to verify the step heights and number of layers by Raman or Raman/PL spectroscopy on individual nanosheets. We reason that this is probably a result of residual solvent on top and below nanosheets, as well as potentially trapped solvent between the layers widening the interlayer distance. In addition, accurate height measurements on inhomogeneous samples (such as nanosheets partially covered with solvent) using AFM tapping mode are generally challenging, as capillary forces and adhesion depend strongly on the material and scanning parameters.^{18, 19}

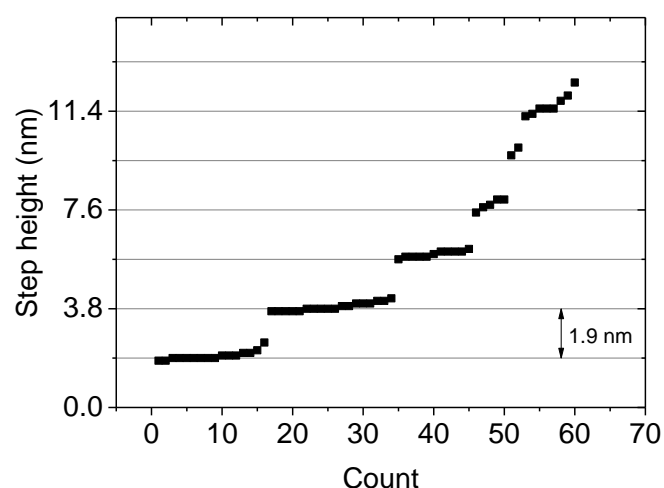


Figure S6: Step height analysis plot for WS₂-SC. Heights of >60 steps of deposited LPE WS₂ nanosheets plotted in ascending order. The step height is always found to be a multiple of a discrete value (in this case 1.9 nm) which is the apparent height of one monolayer measured with AFM (using our scanning parameters, see methods).

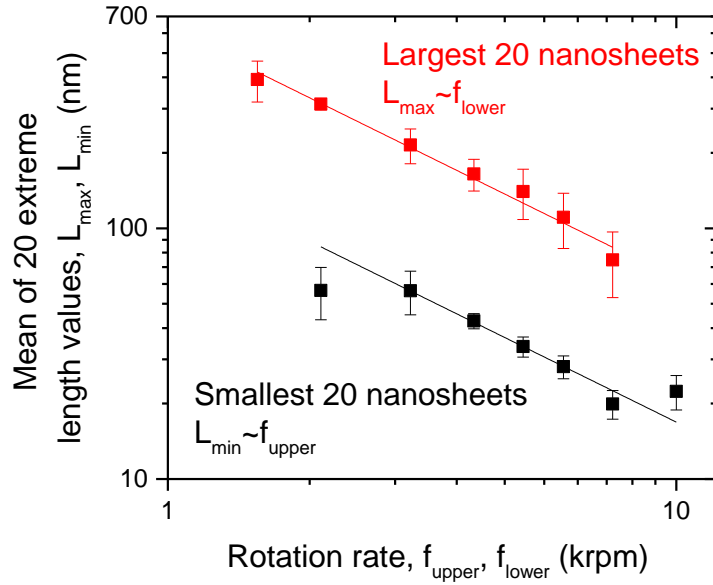


Figure S7: Nanosheet cut-size. Plot of the mean (corrected) AFM lengths of the 20 smallest and largest nanosheets as a function of central g -force of the size selection cascade. According to Peukert *et al.*²⁰ the “cut-size” is the maximum particle diameter which remains dispersed after a centrifugation run and is proportional to $1/f$, where f is the rotation rate. For the cascade shown in Figure 1 (see main text), the length of the largest nanosheets in a given sample is set by the cut size associated with the lower rotation rate while the length of the smallest nanosheets in a given sample is set by the cut size associated with the higher rotation rate. Here, we associate the particle diameter with the nanosheet length. Because $g - force \propto f^2$, this means $L_{\max} \propto f_{\text{lower}} \propto (g - force)_{\text{lower}}^{1/2}$ and $L_{\min} \propto f_{\text{upper}} \propto (g - force)_{\text{upper}}^{1/2}$. The expected behavior is shown above. The fact that the curves don’t overlap shows that the centrifugation cut-off is not sharp presumably due to the rather short centrifugation runs (see Figure S9).

Correction of the measured AFM length

In general, the measurement of lateral sizes is over-estimated in AFM opposed to TEM (see figure 2I main manuscript). This is due tip broadening effects on the one hand and the result of the resolution, which depends on the number of pixels of the image on the other hand. While tip broadening effects are expected to overestimate the lateral size by a constant factor, the broadening due to pixilation will depend on the image size and resolution used. Throughout this study, 512 lines were scanned for each image. However, the field of view was adjusted to the size of the nanosheets. For example, $4 \times 4 \mu\text{m}^2$ areas were scanned in the case of larger nanosheets, while $1 \times 1 \mu\text{m}^2$ areas were scanned for the smaller sizes. Hence, the determined AFM $\langle L \rangle$ is overestimated by a constant factor due to the tip broadening and a factor which is dependent on the lateral size of the nanosheets. To determine the volume fraction of monolayers as accurately as possible, we have corrected the lateral dimensions measured by AFM through the remainder of the study with the empirical relation shown in Figure S8 where we plot the mean length $\langle L \rangle$ measured by AFM *versus* $\langle L \rangle$ measured by TEM. The data can be fitted to a linear function with a slope of 1.21 and an intercept of 6 nm. We argue that the slope is due to the pixilation, while the intercept is a result of the tip broadening. The corrected AFM length is therefore related to the measured length by $L_{\text{corrected}} = L_{\text{measured}}/1.21 - 6 \text{ nm}$. We note that this is not a general relation, but related to instrument, scanning parameters and type of cantilever.

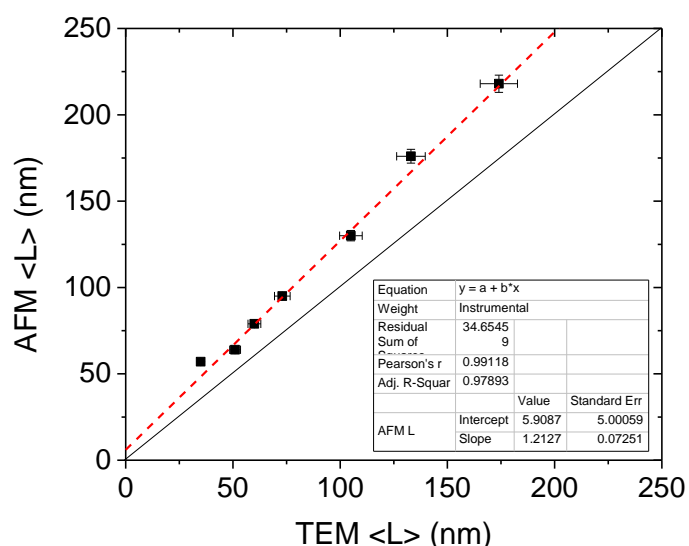


Figure S8: Correction of the measured AFM length. Plot of AFM $\langle L \rangle$ *versus* TEM $\langle L \rangle$ for a number of dispersions. The lateral dimensions from AFM are overestimated due to tip broadening and pixilation. The red dashed line is an empirical fit which we use to correct the

AFM length. We attribute the intercept of 6 nm to tip broadening and the slope of 1.21 to pixilation.

Lateral sizes of N-mers in samples

To further gain insights in the size selection of the LCC, we have analyzed the lateral dimensions expressed as mean L for nanosheets of a given thickness. This data is shown in Figure S9. We find that the mean length of the nanosheet is roughly constant within one sample for different thicknesses except for the sample containing the largest, thickest nanosheets (1.5-2 krpm). This is interesting, as it shows that the applied centrifugation is a length separation process in first approximation and does not separate the nanosheets by mass. If mass separation occurred, the mean length of thinner nanosheets should be larger compared to thicker nanosheets. This suggests that equilibrium in the centrifugation was not reached after the relatively short centrifugation times of 2h in each step. In such cases, back diffusion and friction can play a prominent role and lead to unexpected size selection which is not governed by nanosheet mass. More studies will be required to fully understand the sedimentation process of the 2D systems which is beyond the scope of the current manuscript.

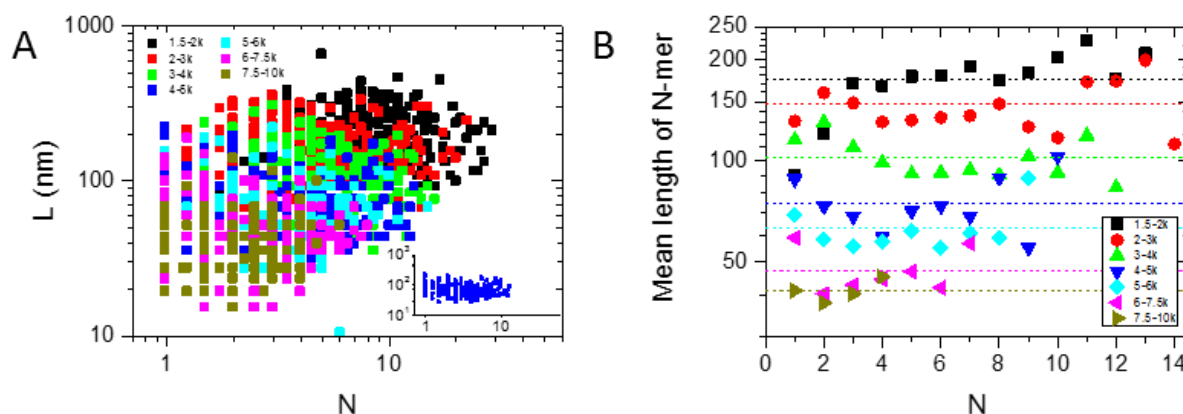


Figure S9: Mean length of N-mers from standard LCC. A) Flake by flake plot of (corrected) nanosheet length *versus* thickness. B) The (corrected) AFM mean length of nanosheets with a certain thickness of 1-10 layers are plotted *versus* the number of layers for the standard size selected samples. The dashed lines are the mean lengths of the WS₂ nanosheets in each dispersion. While nanosheets isolated at lower rpm are thicker and larger in mean (compare Figures S1 and S4), the length does not vary systematically across nanosheets with a given thickness within one size-selected dispersion.

1.3 Extinction coefficient and produced masses

Determination of the extinction coefficient

Since optical extinction spectra of liquid exfoliated transition metal dichalcogenides are known to change as function of size and thickness,¹ it is important to determine size dependent extinction coefficients to accurately measure nanosheet concentration. To do this, we have prepared a number of WS₂ dispersions with varying sizes and thicknesses by changing post-exfoliation centrifugation conditions similar to the procedure described in the methods section of the main manuscript and measured optical extinction spectra. The concentration of WS₂ was then determined by filtration and weighing (alumina membranes pore size 0.02 μm). Prior to weighing, the samples were washed with 600 mL of deionised water and dried in vacuum at 70°C. The thus determined concentration was used to convert the extinction spectra to coefficient spectra as shown in Figure S10.

The extinction coefficient spectra show pronounced changes as a function of nanosheet size (see Figure S10A). As outlined previously for MoS₂¹ and discussed in the main manuscript, the nanosheet size and changes in extinction spectra due to size effects can be expressed as extinction intensity ratio. For WS₂ we use the intensity ratio $\text{Ext}_A/\text{Ext}_{290\text{ nm}}$. In Figure S10B we plot the extinction coefficient at the A-exciton as a function of this peak intensity ratio. This gives the size dependent extinction coefficient at the A-exciton which was used to convert extinction spectra to the respective extinction coefficient spectra.

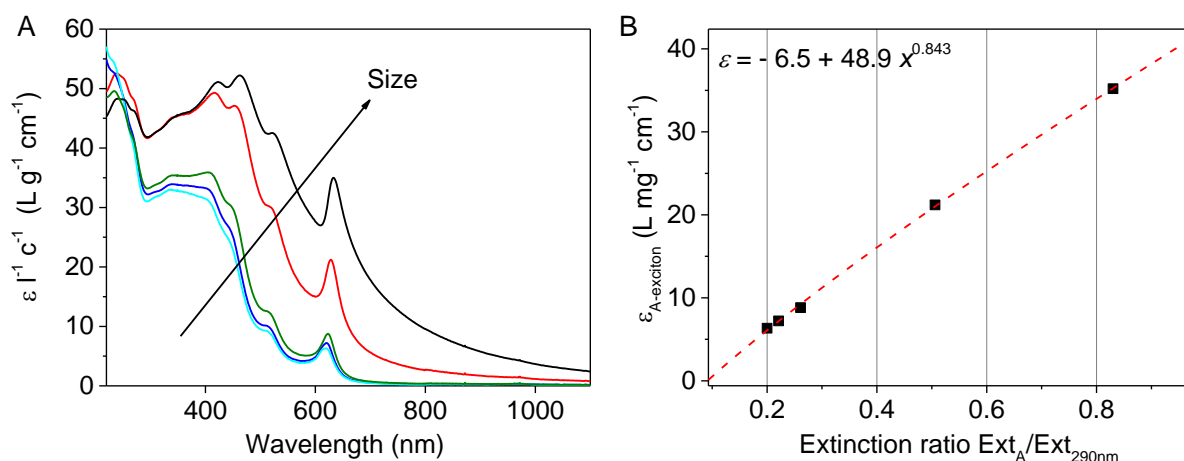


Figure S10: Size dependent extinction coefficient. A) Extinction coefficient spectra of WS₂ exfoliated in an aqueous solution of sodium cholate for different mean nanosheet sizes and thicknesses. B) Extinction coefficient at the A exciton as a function of extinction peak intensity ratio at the A exciton / 290 nm. The dashed line is a fit to the equation shown as inset.

Extinction, absorbance, scattering coefficient spectra

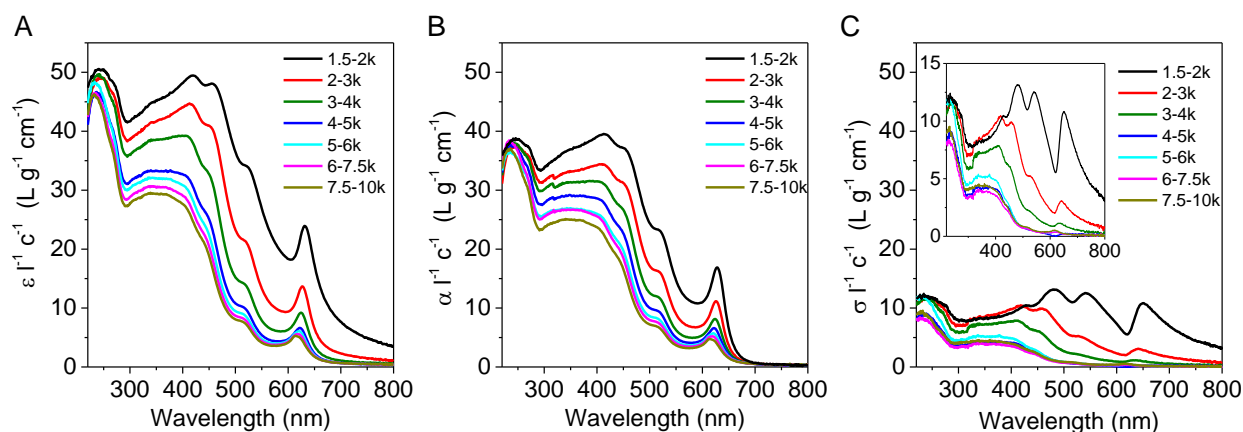


Figure S11: Extinction, absorbance and scattering coefficient spectra. It is known that scattering can contribute significantly to the measured extinction in the case of nanomaterial dispersions.^{1, 21} The real absorbance of the WS₂ dispersions was acquired by measurement inside an integrating sphere, where all potentially scattered light is collected. The cuvette was placed in the center of a 150 mm integrating sphere (Perkin Elmer Lambda 650 spectrometer). The scattering spectra can be calculated as Extinction-Absorbance. A) Extinction coefficient spectra of the size-selected WS₂ dispersions, B) Absorbance coefficient spectra. C) Scattering coefficient spectra. Scattering becomes negligible for WS₂ nanosheets < 100 nm (~3-4k sample). In addition, similar to MoS₂,¹ the scattering spectra follow the absorbance spectra in shape (see inset) in the resonant regime so that information encoded in the absorbance spectra (such as length and thickness) can be extracted from extinction spectra.

2 UV-Vis <L> and <N> metric

2.1 Alternative L metrics

The length metric shown in Figure 4C of the main manuscript can be used to quantify the mean length of exfoliated WS₂ in particular for small nanosheets. However, sometimes, solvents or surfactants may absorb light in the UV region making an accurate determination of the WS₂ extinction at 235 nm impossible. In these cases, we propose that the extinction at the A exciton / the local minimum at 290 nm Ext_A/Ext₂₉₀ (see Figure S121A) can be used as metric according to equation S1.

$$L = \frac{1000Ext_A / Ext_{290} - 7.6}{2.8} \quad (\text{eq. S1})$$

We note that this metric breaks down for nanosheets with a mean length < 60 nm.

In addition, we have found that the ratio Ext_A/Ext₂₉₀ (see Figure S12B) which relates to the nanosheet length according to equation S2 is more robust over a wider size range, as the error is smaller due to bigger changes in the spectral shape. However, for both alternative metrics, the fit parameters would imply negative extinction coefficient at edge sites. Equations S1 and S2 therefore do not have any physical meaning and are to be considered purely empirical relationships.

$$L = \frac{1000Ext_A / Ext_{235} - 28.5}{1.1Ext_A / Ext_{235} + 1.6} \quad (\text{eq. S2})$$

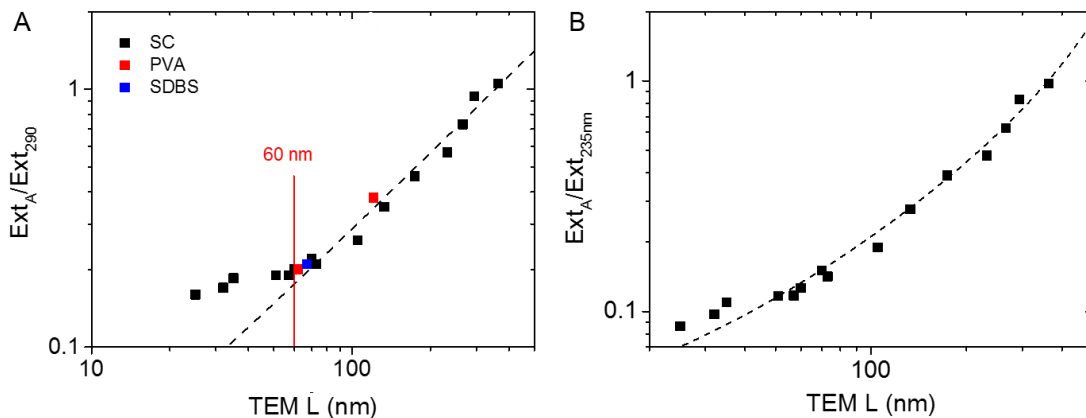


Figure S12: Alternative L metrics. A) Ratio of extinction at the A-exciton to that at 290 nm plotted *versus* mean nanosheet length, as measured by TEM. The dashed line describes eq S1. The metric breaks down for nanosheets with $L > 60$ nm. B) Ratio of extinction at the A-exciton to that at 235 nm plotted *versus* mean nanosheet length, as measured by TEM. The dashed line describes eq S2.

2.2 Second derivatives of extinction spectra to obtain $\langle N \rangle$

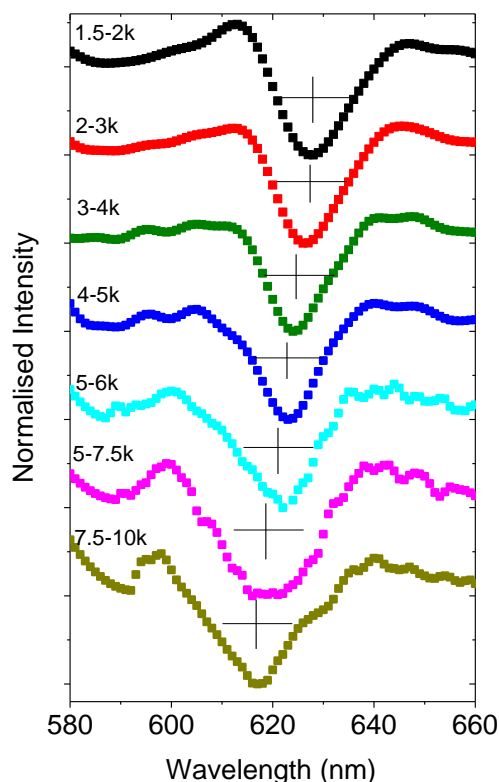


Figure S13: Smoothed second derivatives of the A exciton extinction spectra of the standard size selected samples. The spectrum was first differentiated and then smoothed with the Adjacent Averaging Method (20-30 points). We found this smoothing method most suitable to estimate the center of mass position. We define the center of mass peak position as the wavelength at the full width of half maximum of the peak in the smoothed second derivative. This position is indicated by the cross in the figure. We note that the term “center of mass position” is technically not correct, as it usually assumes symmetrical peak shape which is not the case here. However, it describes the idea of the methodology of taking the wavelength associated with the full width of half maximum of the peak quite well. The as-determined center of mass position is plotted *versus* layer number in the main manuscript (see main text F4D) to give the empirical metric for the mean number of layers of the exfoliated WS₂.

2.3 Optical characterization of very small nanosheets discarded in the primary cascade

In our standard size selection cascade, we remove all nanosheets that are retained in the supernatant after 10 krpm. We nonetheless characterized the majority of this material by trapping the nanosheets sedimenting between 10 and 15 krpm. TEM shows that the material consists of small, but 2D nanosheets (figure S2). The optical extinction spectra (figure S14A) also show now apparent or unexpected differences compared to the larger nanosheets. To obtain the length metrics, samples produced in such a way were therefore added to the extinction ratio *versus* $\langle L \rangle$ plots yielding the well-defined relationships observed. Unfortunately, the limited size made an AFM analysis extremely challenging giving no reliable data. However, the PL/Raman measurements (figure S14B) revealed that these very small nanosheets have optical properties distinct from their larger counterparts. Notably, the PL/Raman ratio is lower compared to the sample produced from centrifuging between 7.5-10 krpm (2.4 in the case of the 10-15 krpm sample compared to ~ 4 in the case of the 7.5-10 krpm sample). In addition, a background signal at lower wavelength is observed and the PL appears broadened and more asymmetric. This strongly suggests that edge effects have an impact on the photoluminescence properties of the liquid exfoliated WS₂ and ultimately made us discard these nanosheets throughout this manuscript. The size issue is addressed in more detail further down below (figures S33-34).

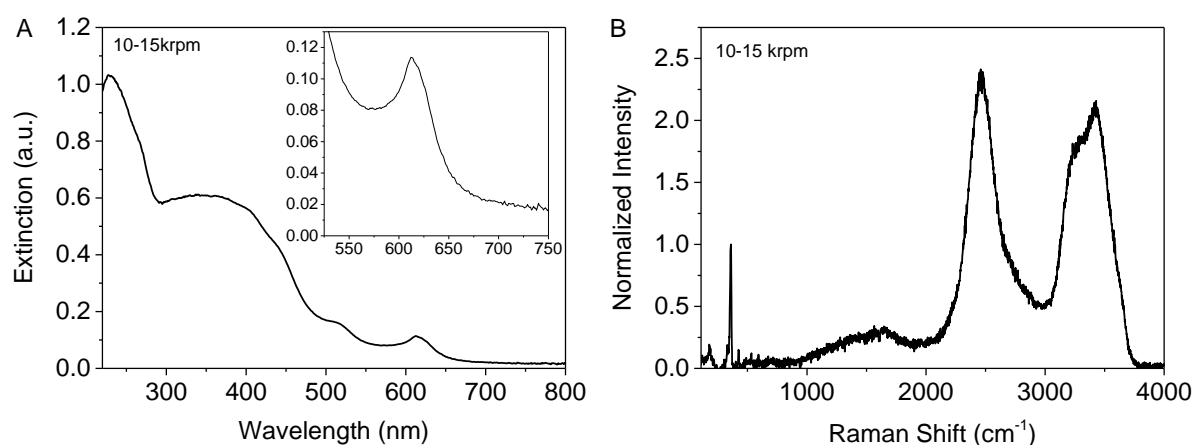


Figure S14: Optical characterization of very small nanosheets discarded in the standard size selection cascade. A) Optical extinction spectrum with the A-exciton region shown in the inset. No striking deviation from larger nanosheets is observed. B) PL/Raman spectrum measured on the surface of a liquid drop of the 10-15 krpm sample. Acquisition parameters were identical to the sample shown in the main manuscript. PL/Raman ratios are lower than expected and additional signal is observed in the region of 1000-2000 Raman shift.

3 Further examples of fitted PL spectra

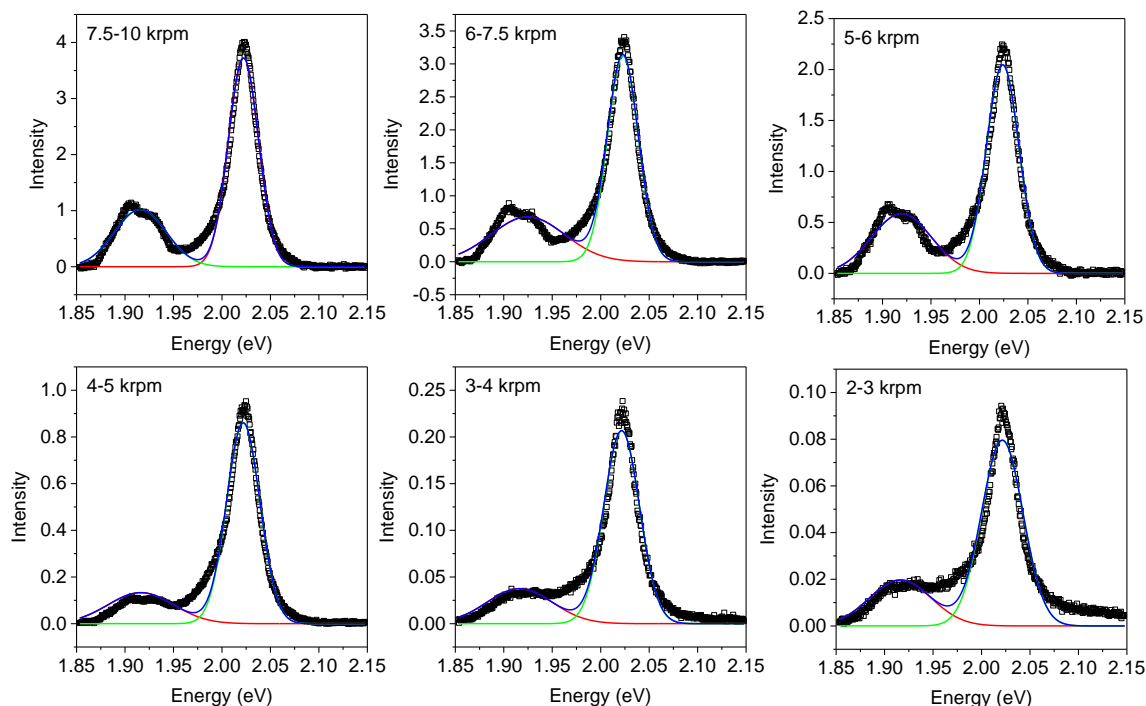


Figure S15: Examples of fitting the PL to Gaussians for a number of size-selected samples as indicated in the figure legend. We consistently find worse fits than with Lorentzians. This may be due to the presence of trion emission at lower energy from the main exciton component. However, due to the Raman peak of water in the close proximity and uncertainties in correcting the baseline, this cannot be resolved in the case of these spectra. However, Figure S32 shows a PL spectrum that was recorded at an excitation wavelength of 450 nm. In this case, the PL spectrum can be fit very well to two Gaussians attributed to exciton and trion to a very minor extent. This confirms that the WS₂ nanosheets in aqueous surfactant solutions are widely undoped in contrast to nanosheets deposited on Si/SiO₂ wafers (see Figure S18).

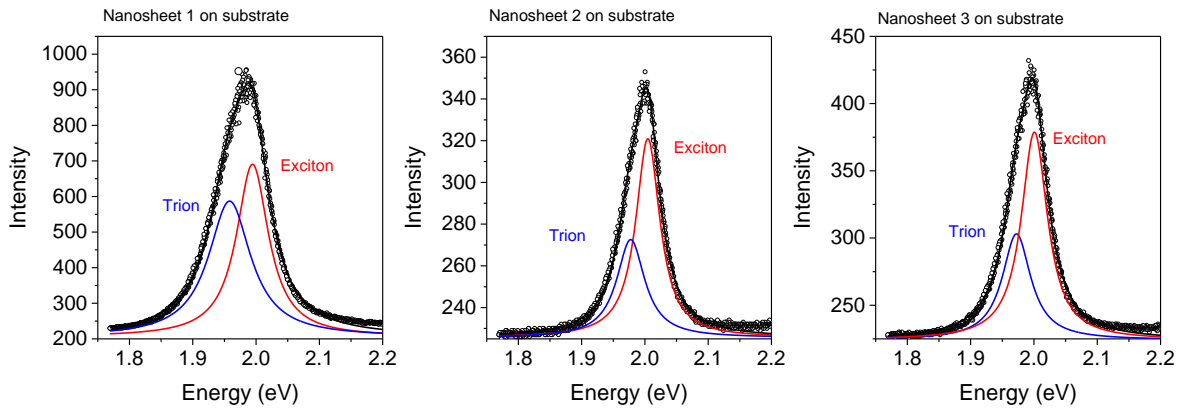


Figure S16: Fitted PL spectra of individual monolayers after deposition on a Si/SiO₂ substrate. Since peak positions and widths of the photoluminescence from monolayered TMDs are highly sensitive both to the quality of the material and the dielectric environment, we deposited individual nanosheets on Si/SiO₂ substrates to have a better comparison to the state of the art materials described in literature. In contrast to the PL spectra measured in liquid, a single Lorentzian does not describe the peak well. However, the spectra can be fit very well to two Lorentzian lines attributed to exciton emission and trion emission at slightly lower energy due to doping from the substrate.²²⁻²⁴ This seems to be compensated in the liquid presumably due to water in the vicinity of the nanosheets²² so that emission from trions is negligible. This observation is also consistent with lower exciton emission energies and broader linewidths in the range of 45-60 meV.^{22, 23} However, we note that these linewidths on the substrate are still consistent with high quality nanosheets on Si/SiO₂.²⁵⁻²⁷

4 Robustness of metrics towards stabilizer concentration

It is important to test whether the quantitative spectroscopic metrics established are widely applicable. One parameter that may have an impact due to solvatochromic effects is the concentration of the stabilizer. For this purpose, we have redispersed a WS₂-SC dispersion trapped between 3-5 krpm in SC of varying concentrations ranging from 0 (pure water) to 5 g/L to yield dispersions with WS₂ concentrations of ~ 1 g/L in each case. This experiment served a dual purpose. i) to confirm the robustness of the quantitative metrics and ii) to demonstrate the exfoliated and size-selected nanosheets can be redispersed even in water at reasonably high nanosheet concentrations with minimal stabilizer present.

The resultant extinction and Raman/PL spectra are shown in figure S17. It is clear that they are virtually identical except for an increased extinction below 220 nm due to varying concentrations of SC (spectra were acquired with water as baseline). As a consequence of the identical spectra, the results from the analysis of the metric values (concentration, length, thickness and ML content from Raman/PL) do not change with the surfactant concentration as shown in figure S18.

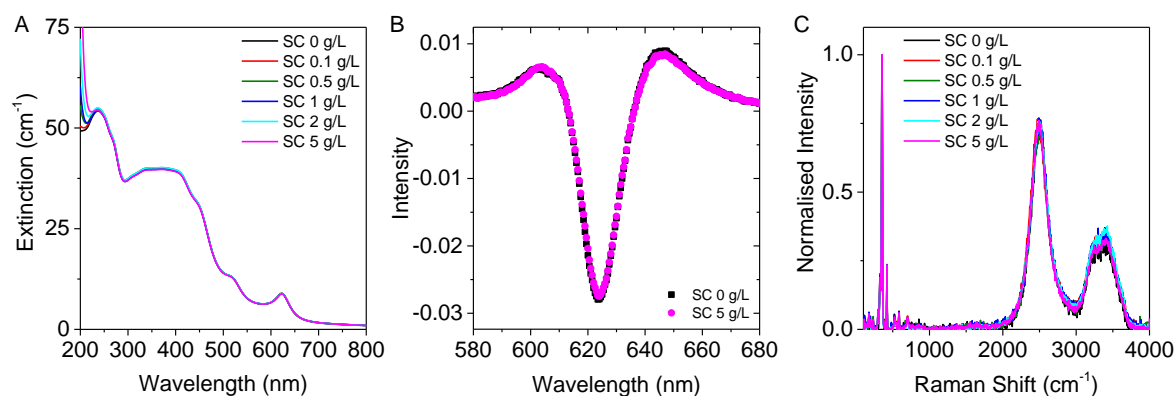


Figure S17: Extinction and Raman/PL spectra of WS₂ redispersed in aqueous SC with varying SC concentrations. A) Extinction spectra, B) Smoothed second derivative of the A-exciton of the samples redispersed at highest and lowest SC concentration, C) Liquid Raman/PL spectra (excitation 532 nm) normalized to the main WS₂ Raman mode.

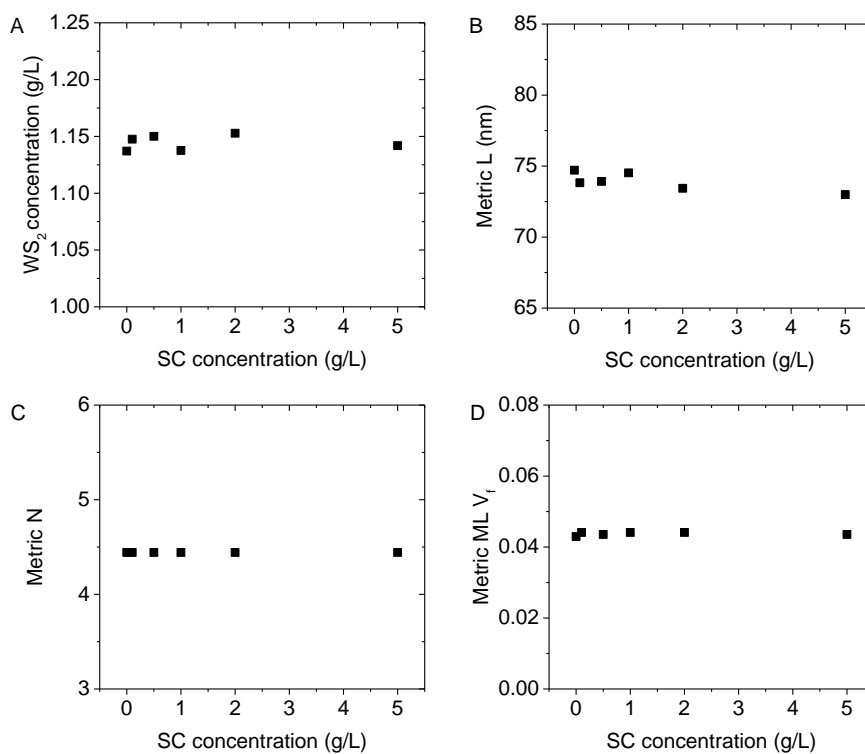


Figure S18: Robustness of metrics towards stabilizer concentration. Shown are the results of the metric analysis plotted as a function of SC concentration used to collect the WS₂ after centrifuging at a given set of rpms (3-5 krpm). A) WS₂ concentration (from the size-independent extinction coefficient at 235 nm), B) Nanosheet length (from the intensity ratio Ext₂₃₅/Ext₂₉₀), C) Nanosheet thickness (from the A-exciton center of mass position, D) Monolayer volume fraction (from the PL/Raman intensity ratio).

5 Comparison different centrifugation procedures

Comparison LCC size selection to homogeneous centrifugation

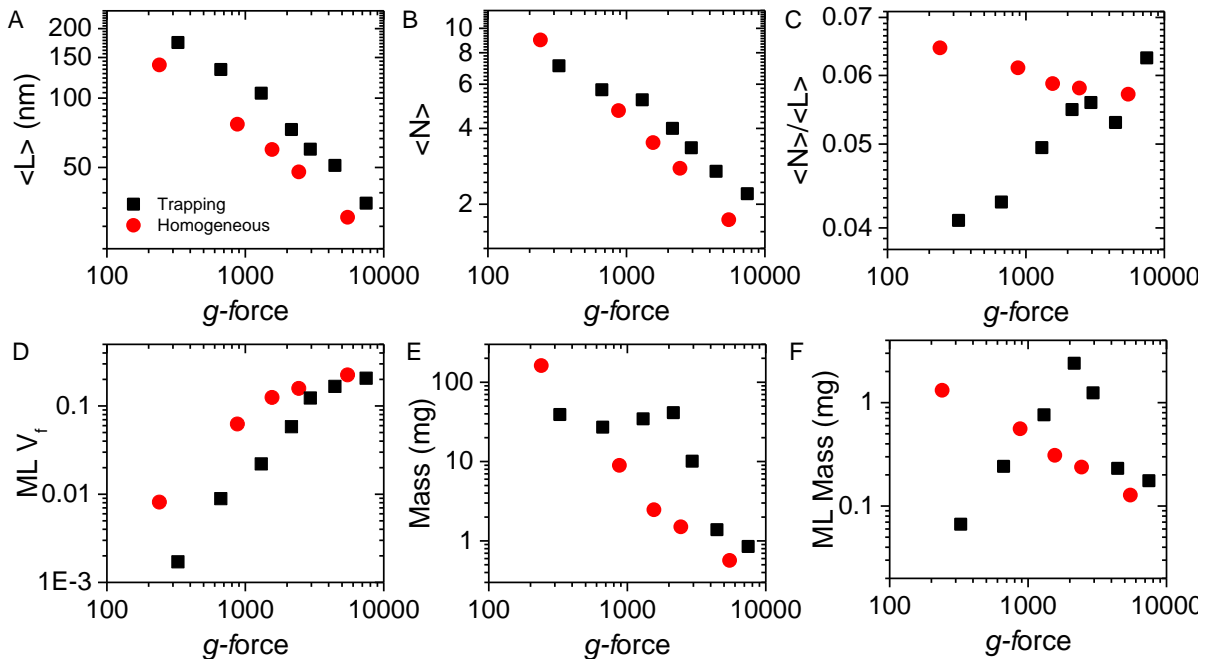


Figure S19: Comparison of LCC trapping size-selection and homogeneous centrifugation at different centrifugation rates. The data is plotted as a function of g -force. In the case of homogeneous centrifugation, this represents the actual centrifugation speed, while in the case of the trapping between rpm cascade, the central speed is chosen. The data for the LCC was extracted from microscopy statistics, while the metrics were used in the case of the homogeneous centrifugation. We note that microscopy statistics are extremely challenging from samples produce by homogeneous centrifugation, as small nanosheets are not removed and samples are hence more polydisperse. A) Mean nanosheet length *versus* g -force showing a decrease in nanosheet size with increasing centrifugation speed. B) Mean nanosheet thickness *versus* g -force showing a decrease in nanosheet thickness with increasing centrifugation speed. In general, mean sizes (length and thickness) are smaller for samples produced by homogeneous centrifugation, as the smallest nanosheets were not removed. C) Thickness/length aspect ratio as a function of centrifugation speed. The aspect ratio is widely constant for the homogeneous centrifugation, but increases in the case of the LCC size-selection. D) Volume fraction of monolayers *versus* g -force. In both cases, V_f increases monotonically, albeit less steeply for the homogeneous centrifugation suggesting ML enrichment is less efficient. E) Total mass of WS_2 and F) monolayer mass of WS_2 collected in each sample. In the case of the homogeneous centrifugation, the sample was split in equal

aliquots which were centrifuged at different speeds. The respective sediments were discarded so that the overall yield is lower.

Size selection cascade of WS₂ exfoliated in NMP

To demonstrate the broader applicability of the LCC, we performed LCC on WS₂ exfoliated in solvent rather aqueous surfactant solution. Samples were produced from sonication in the common solvent *N*-methyl-2-pyrrolidone (NMP) with all other parameters being kept identical. The cascade was performed as described in the supplementary methods. Figure S20A shows the measured extinction spectra with similar variations as in the case of the cascade in water-SC being apparent. The second derivative of the A-exciton (Figure S20B) also shows expected shifts in the A-exciton with nanosheet thickness albeit less pronounced than in SC.

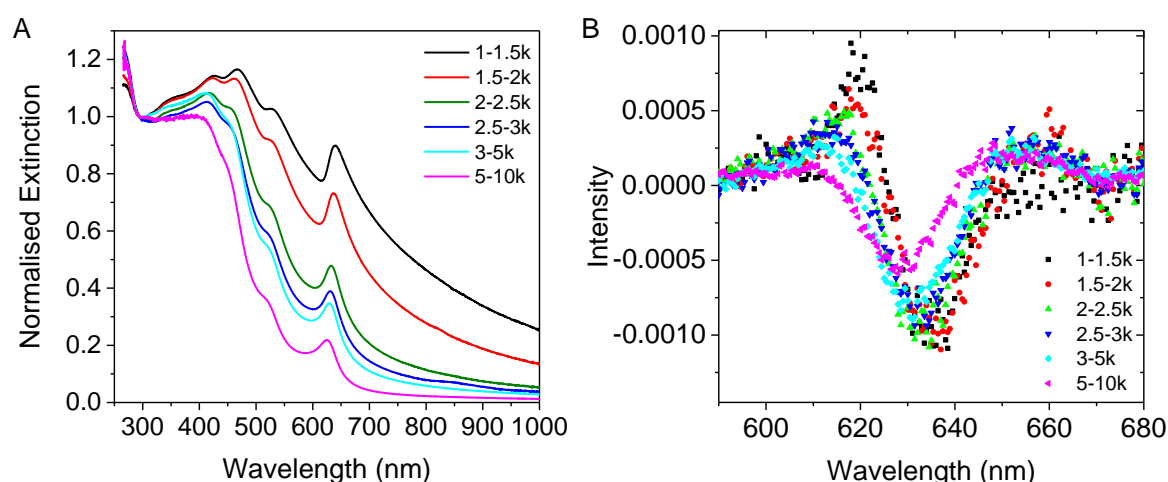


Figure S20: Optical characterization of a LCC of WS₂ exfoliated and size-selected in NMP. A) Full extinction spectra normalized to the local minimum. B) Smoothed second derivatives of the A-exciton.

A disadvantage of using NMP as a solvent is its absorbance in the UV region making wavelengths < 270 nm inaccessible. This is problematic for two reasons: i) the size independent extinction coefficient at 235 nm cannot be used to determine the concentration. Instead, size dependent extinction spectra need to be used in analogy to the procedure described in figure S10. ii) The robust length metric that also holds for small nanosheets involves the extinction at 235 nm and can thus not be applied. Instead, the alternative metric Ext_A/Ext_{290} (see equation S1) must be taken which breaks down for nanosheets < 60 nm. We note that therefore, we have shifted the rpms in the LCC towards lower rpms to collect slightly larger nanosheets compared to the LCC in SC. In addition, liquid Raman/PL in NMP cannot easily be performed, as the Raman modes of NMP overlap partly with the WS₂ PL at 532 nm excitation.

We can nonetheless compare the dispersed concentration, as well as the Ext_A/Ext_{290} length metric and A-exciton center of mass position to the result obtained from an LCC in SC. These parameters are plotted *versus* the median g -force in figure S21. The dispersed concentration, *i.e.* mass produced is lower in each fraction compared to SC. This strongly suggests less efficient dispersion in NMP compared to SC under equal sonication conditions. The plot of the Ext_A/Ext_{290} length metric (figure S21B) in turn suggests that the nanosheets in NMP are consistently larger, while the consistently larger A-exciton positions (figure S21C) suggest they are also thicker in each fraction. While this is entirely possible due to a different exfoliation and stabilization, it could also be an effect related to solvatochromism which may result in changes in the spectral shape.

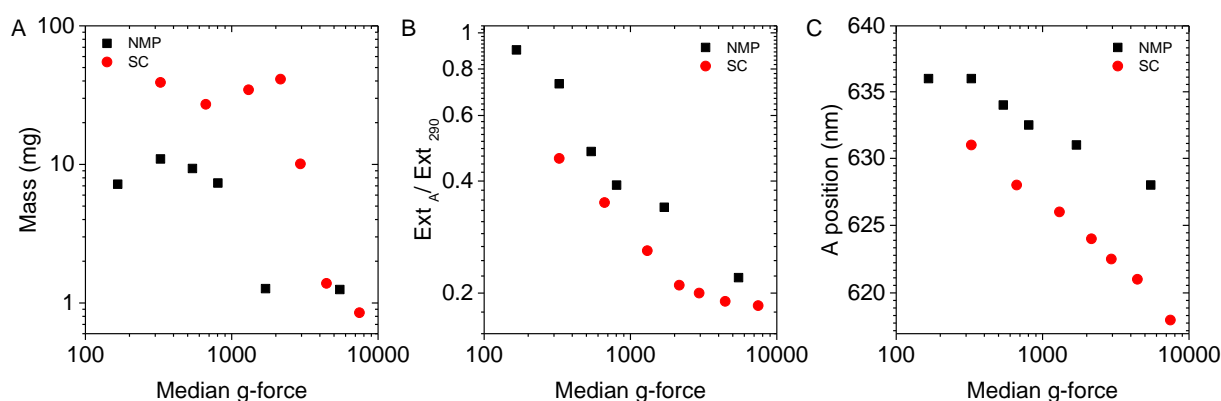


Figure S21: Mass, length and thickness metric of LCC in NMP compared to H₂O-SC. A) Mass in each fraction plotted as function of median g -force. B) Extinction length metric Ext_A/Ext_{290} as function of median g -force and C) A exciton position.

To address this, we have transferred the samples produced and size-selected in NMP to water-SC. This was possible by high speed centrifugation, washing with water-SC and a second high speed centrifugation after which the sediments were collected in water-SC (SC concentration of 2 g/L). Unlike the redispersion from LCC, agitation by shaking was not sufficient for a complete redispersion and mild sonication (5 min bath) was used. The great advantage of this transfer is that the full UV-Vis spectrum becomes accessible and Raman/PL spectra can be acquired. The resultant spectra are shown in figure S22. We would like to note that the PL/Raman ratio is significantly lower than from samples directly produced in SC. However, there are no apparent shifts or other changes to the PL so we attribute this to a lower monolayer content due to poorer exfoliation in NMP rather than solvatochromic effects from traces of NMP that may still be in the samples.

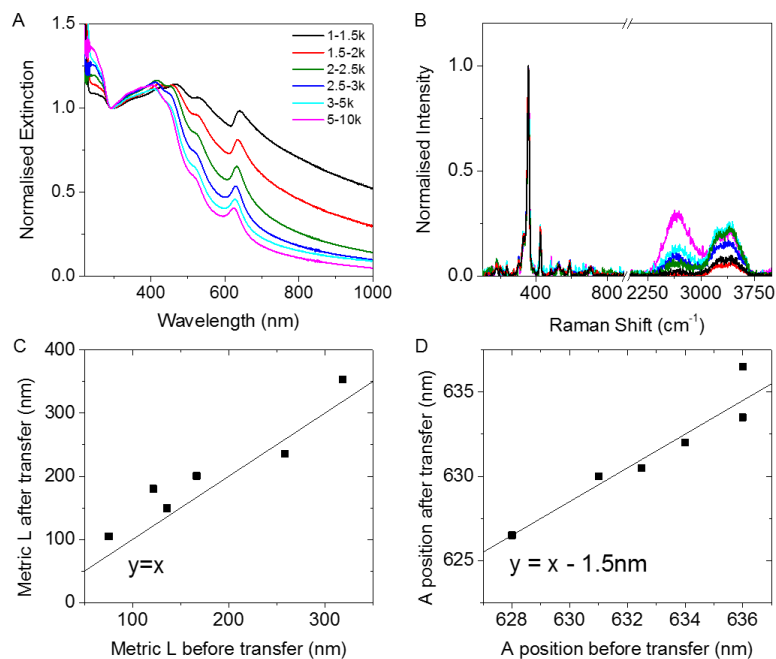


Figure S22: Spectroscopic characterization of WS₂ exfoliated and size selected in NMP after transfer to water-SC. A) Extinction spectra normalized to the local minimum, B) PL/Raman spectra normalized to the main WS₂ Raman mode (excitation 532 nm), C) Metric length after transfer plotted as a function of metric length before transfer, D) A-exciton position after transfer plotted as a function of A-exciton position before transfer.

In figure S22C and D, we plot the metric values against each other before and after transfer to test whether significantly different values for length and thickness are obtained when applying the established metrics to a solvent system. The length metric (figure S22C) certainly is applicable and gives the same result in NMP compared to SC (within error considering that the Ext_A/Ext_{290} metric is used for the samples in NMP and the more reliable metric Ext_{235}/Ext_{290} is used for water-SC). Figure S22D shows that care must indeed be taken when using the A-exciton center of mass position as thickness metric, as the results after transfer from NMP to SC are offset by ~ 1.5 nm as indicated by the straight line. Such an offset corresponds to a deviation of 1-2 layers. This suggests a new metric is needed which we give below.

The transfer to SC can be used to directly compare the exfoliation and LCC in NMP to our standard procedure in SC. The result plotted as a function of median g -force is summarized in figure S23. Except for the smallest nanosheets, the data from LCC in NMP collapses on the same curve as for SC (figure S23A). This demonstrates that this primary LCC is predominantly governed by nanosheet length (even though thickness also changes).

The deviation at high centrifugal forces is likely predominantly related to the fact that the population of nanosheet sizes and thicknesses is different in the stock dispersion after exfoliation in NMP and SC, respectively. In contrast, the thickness data for the samples exfoliated in NMP is clearly offset to thicker nanosheets, albeit showing a similar trend (figure S23B). This strongly suggests that nanosheets exfoliated in NMP are simply thicker to begin with and not that the separation mechanism is different. If the latter was the case, the two data sets would not be expected to proceed in parallel. In figure S23C, we compare monolayer volume fractions determined from the PL/Raman spectra. As evident from the spectra, the PL and therefore monolayer volume fraction is significantly lower in the case of the NMP-exfoliated samples.

Shown in figure S23D is a plot of A-exciton wavelength versus mean nanosheet thickness for nanosheets exfoliated in both SC and NMP. The red line represents the metric described in the main text. It can be seen that this metric actually described the NMP-dispersed nanosheets quite well. In fact, applying the SC thickness metric (equation 4 in main ms) to NMP dispersions would be accurate to within better than 20% so long as $\langle N \rangle$ is below 10. This implies that solvatochromic effects, although present, are small enough that equation 4 can be used as a first approximation in any system based on aqueous or organic solvents. Nevertheless, because NMP is such a well-known solvent, we use the data in figure S23D to extract an accurate thickness metric for WS₂ nanosheets in NMP (black line). This allows the thickness of nanosheets in NMP to be estimated and is given by:

$$\langle N \rangle = 5.62 \times 10^{-28} \times e^{\lambda_A/9.74}$$

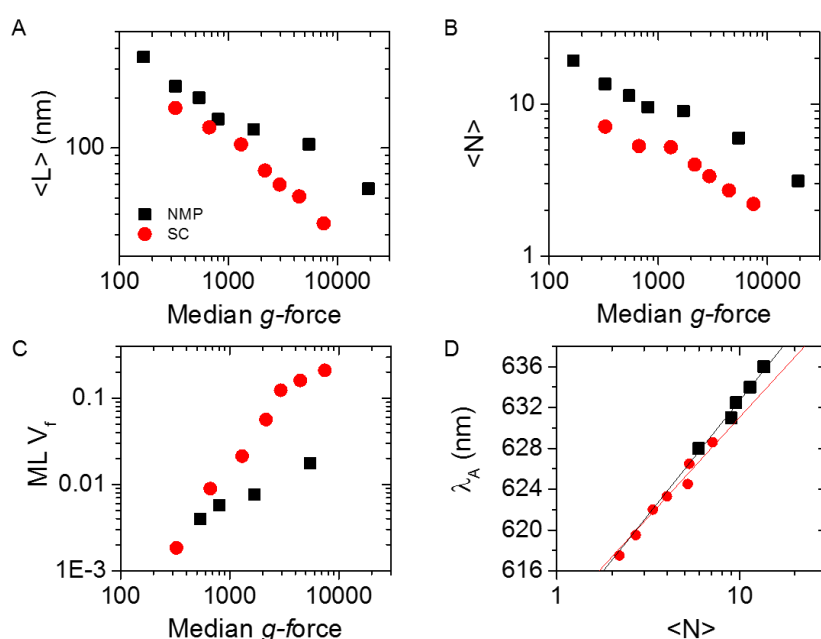


Figure S23: Comparison of LCC in NMP (after transfer to SC) to LCC in SC. All parameters are plotted as function of median g -force. A) Nanosheet length, B) Nanosheet thickness, C) Monolayer volume fraction. D) Wavelength associated with A-exciton, plotted *versus* mean nanosheet thickness for nanosheets exfoliated in NMP and SC. The red line represents the metric described in the main text. The black line represents another metric, described above, which allows the thickness of nanosheets in NMP to be estimated.

Comparison LCC size selection to repeated centrifugation at fixed rotations

A great strength of the LCC is that different cascades can be designed. A simple variation is repeated centrifugation at the same rotational speed. The results of such a procedure is summarized in figure S24.

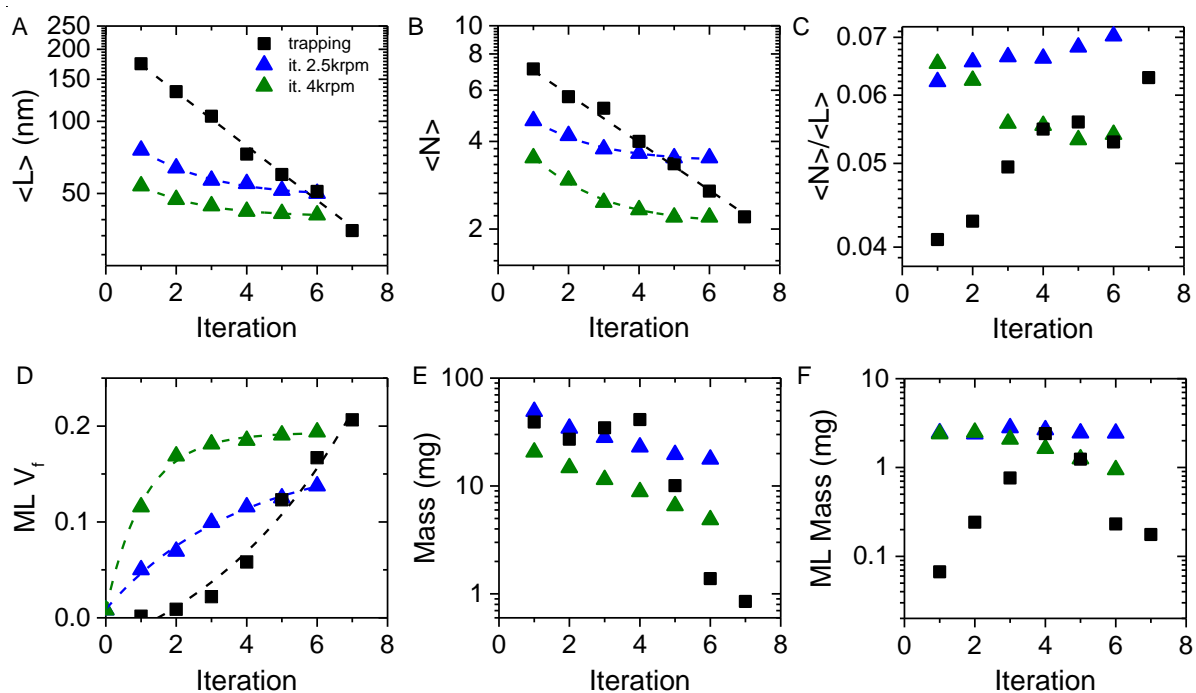


Figure S24: Comparison of the size-selection cascade to repeated centrifugation at two fixed speeds. A) Mean nanosheet length and B) nanosheet thickness plotted as function of iteration step. Repeated centrifugation at a fixed centrifugation speed (2.5 and 4 krpm, respectively) is significantly less efficient to achieve size-selection. C) Thickness/length aspect ratio plotted *versus* cycle number. Interestingly, the aspect ratio slightly increases for the repeated centrifugation at 2.5 krpm, while it decreases in the case of 4 krpm. This is important, as it shows that nanosheets of a given length are becoming thinner. D) Monolayer volume fraction is a function of cycle number. The repeated centrifugation at fixed rpm is highly powerful in enriching the samples in monolayers (while widely maintaining the mean nanosheet size). However, an exponential increase is observed suggesting that saturation is reached at some stage (which is dependent on the centrifugation speed chosen). E) Total mass of WS_2 and F) mass of ML WS_2 as function of cycle number. Total mass falls off comparatively slowly for the repeated centrifugation at a fixed rotational speed. Most importantly, no MLs are lost in the case of the repeated centrifugation at 2.5 krpm.

6 Monolayer enrichment

6.1 General centrifugation procedure

In the following, we have designed a number of secondary cascades with the goal to enrich the dispersions in monolayers in as few centrifugation steps as possible, while widely maintaining reasonable nanosheet sizes. The design is based on the following rationale: We showed in Figure S24 that repeated centrifugation at fixed rotations is highly efficient in increasing the volume fraction of monolayers. However, V_f saturates which makes more complicated cascades necessary to obtain very high monolayer contents. We anticipate that a long centrifugation run (over night) will give a similar trend as repeated centrifugation at fixed rotations at relatively short times of 2 h. If that was the case, a long centrifugation at low speeds such as 2.5 krpm should enrich the dispersion in ML without sacrificing too much ML mass (see Figure S24F). In addition, a long centrifugation run at 4 krpm is expected to decrease the N/L aspect ratio (see Figure S24C) while at the same time further increasing the ML V_f (figure S24C). This is beneficial because we want to avoid that the ML enriched nanosheets become too small with optical properties being dominated by edges. N.B: Edge effects on optical properties are demonstrated and discussed in Figures S33-34. Hence, we combine these long centrifugation runs (typical overnight) at low and intermediate speeds with short high speed centrifugations where very small nanosheets are removed in designed ML enrichments cascades. The general scheme is shown in Figure S25. A few specific examples are presented in the following.

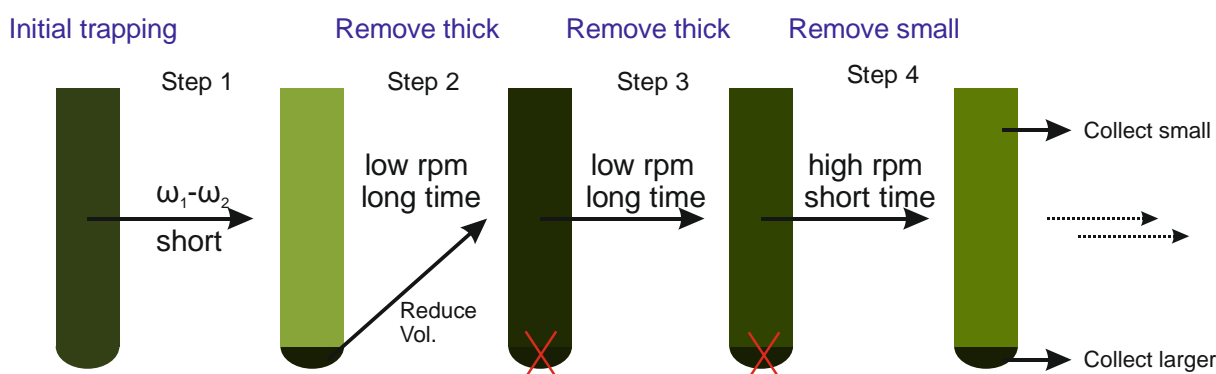


Figure S25: Schematic representation of the ML enrichment centrifugation. After the initial size selection, the samples are centrifuged in further iterations at lower rpm for longer times to remove thicker nanosheets. A centrifugation at higher speeds is required to remove very small nanosheets.

6.2 Example scenario 1: Spectroscopic data and AFM

Spectroscopic data

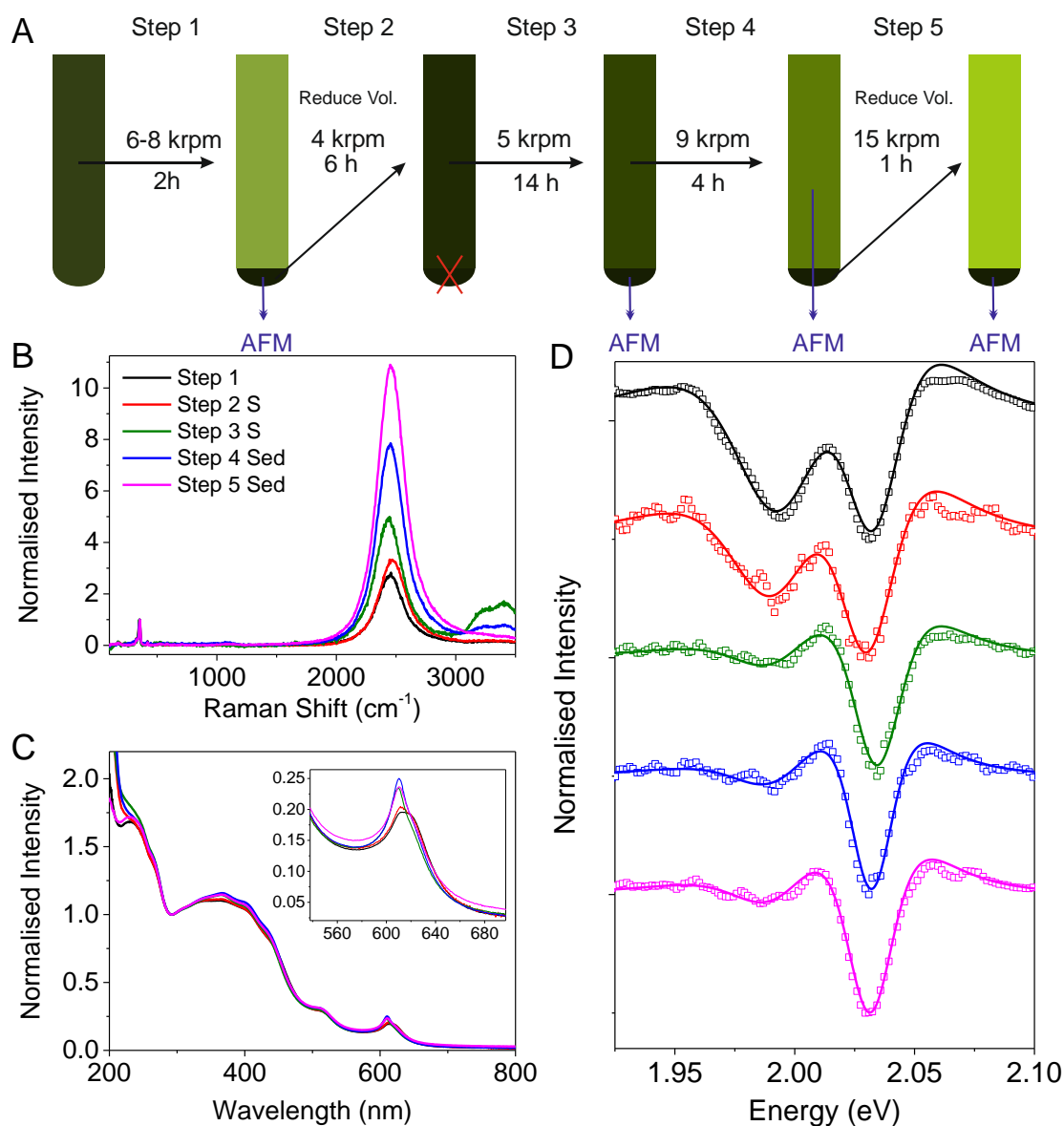


Figure S26: Spectroscopic data of example 1 of the monolayer enrichment. A) Schematic of the centrifugation procedure. A subset of the samples as indicated was subjected to AFM statistical analysis. B) Normalized Raman/PL spectra ($\lambda_{\text{exc}} = 532$ nm) measured on liquid drops of the dispersions after the centrifugation steps as indicated showing the increase in relative PL intensity related to the ML enrichment. C) UV-Vis extinction spectra normalized to 290 nm. Changes in the spectra region 200-250 nm are related to changes in length. Inset: A-exciton. Changes in the shape of the A-exciton are related to varying distributions of ML and FL WS₂. D) Second derivatives of the A-exciton obtained after smoothing the spectrum with the Lowess method (10-15 points). The spectra were fitted to the second derivative of two Lorentzians as described in SI section 5.

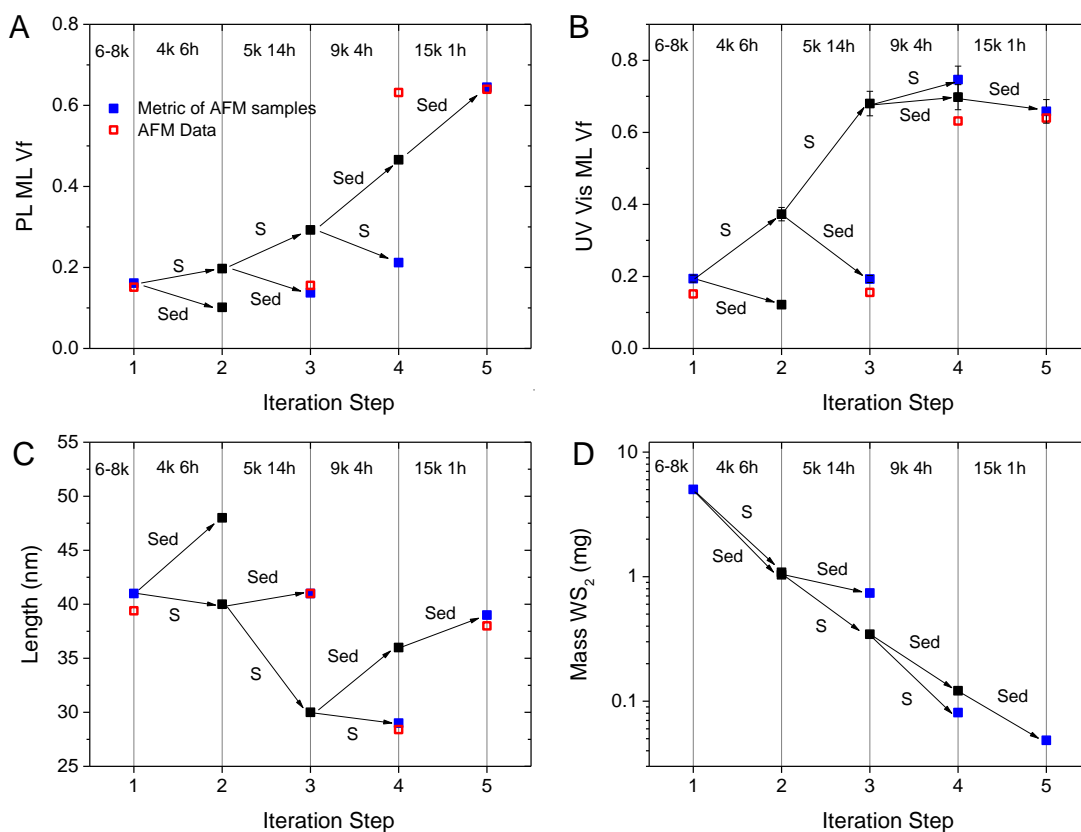


Figure S27: Summary of example 1 of the ML enrichment centrifugation procedure. The rotational speeds and times are indicated at the top of the individual panels. Blue data points indicate the samples that were subjected to AFM. The red data points are the result of the AFM analysis (see Figure S28). A) Volume fraction of monolayers determined from the PL/Raman metric of the supernatants (S) and sediments (Sed) after each iteration step. The supernatant after step 4 shows a strong discrepancy between the volume fraction determined from the PL/Raman metric compared to the volume fraction measured from AFM. This is because the photoluminescence is quenched due to edge effects in very small WS_2 nanosheets (see Figures S33-34). B) Volume fraction of monolayers determined from the UV-Vis A-exciton shape metric of the supernatants (S) and sediments (Sed) after each iteration step. Volume fractions measured from AFM agree very well with values obtained from the metric even for the smallest nanosheets suggesting that the UV-Vis metric is more reliable than the PL/Raman metric in the case of small nanosheets. C) Mean length determined from the empirical UV-Vis peak intensity ratio Ext_{235}/Ext_{290} of the supernatants (S) and sediments (Sed) after each iteration step according to equation 3 in the main manuscript. The (corrected) length from AFM agrees very well with the metric data. D) Mass of WS_2 after each iteration step.

AFM on selected samples

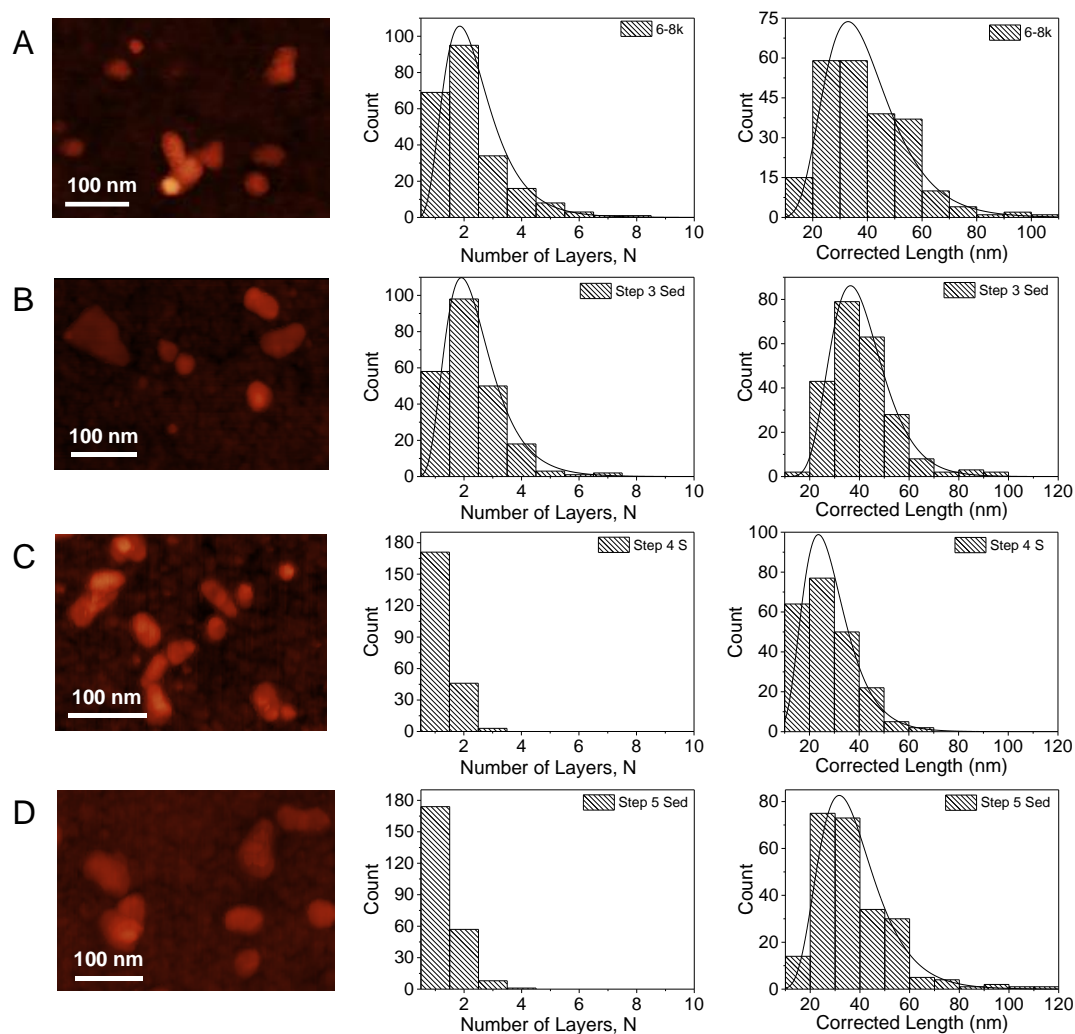


Figure S28: AFM analysis of selected samples of the monolayer enrichment procedure schematically shown in Figure S26A. Left: Representative images, middle panel: number of layer histograms. Right: Histograms of the (corrected) length. A) WS₂ dispersion obtained by the standard size selection centrifuged between 6-8 krpm used as a starting point for the ML enrichment. B) Sediment after step 3. C) Supernatant after step 4. D) Sediment after step 5. This sample shows the highest PL/Raman ratio obtained with this cascade. However, according to AFM, the volume fraction of monolayers is similar to the supernatant after step 4 which has a significantly lower PL/Raman ratio. This is attributed to fluorescence quenching due to edges in very small nanosheets (see Figure S33-34).

6.3 Example scenario 2: Spectroscopic data and AFM

Spectroscopic data

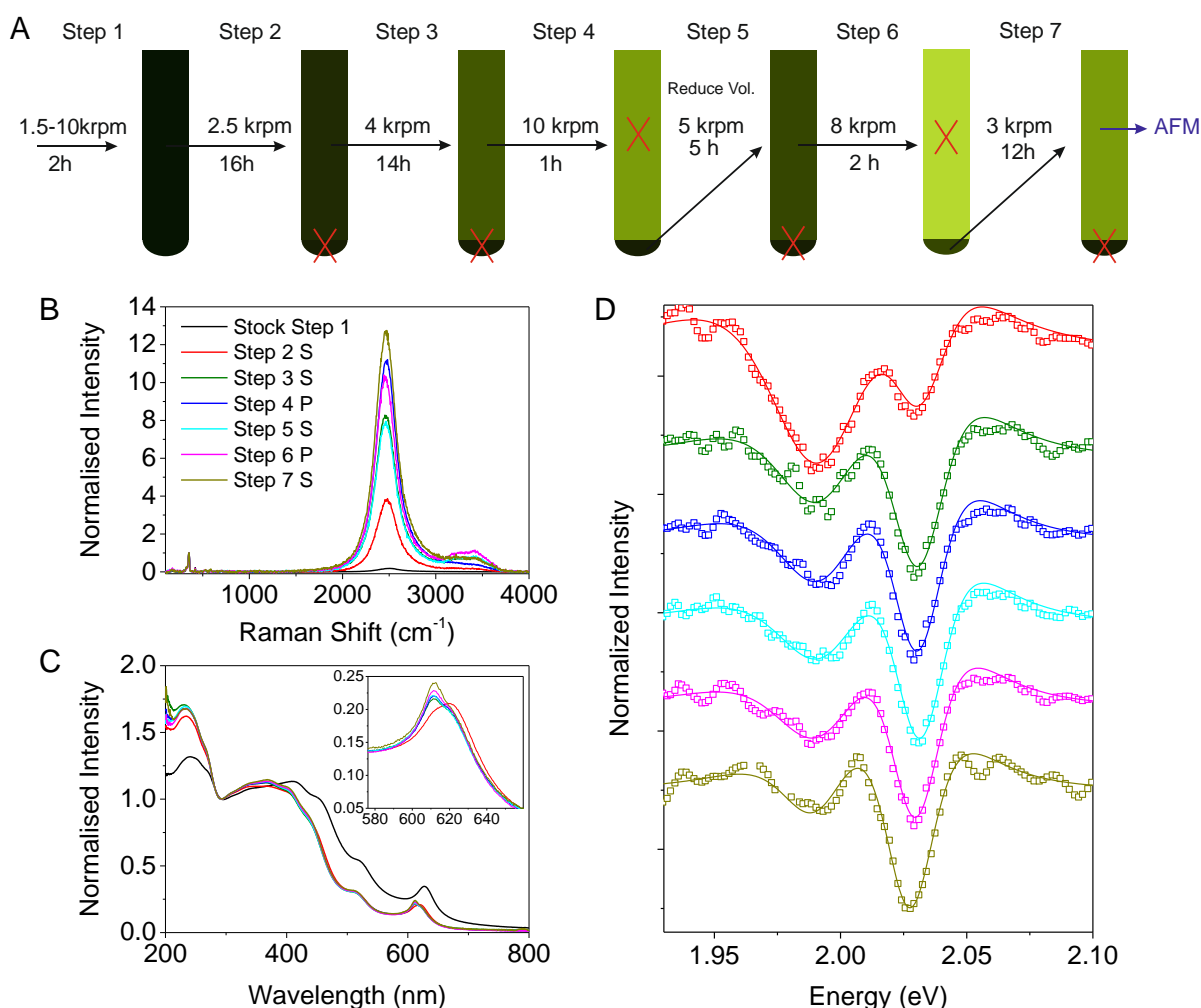


Figure S29: Spectroscopic data of example 2 of the monolayer enrichment. A) Schematic of the centrifugation procedure. The final supernatant was subjected to AFM. B) Normalized Raman/PL spectra ($\lambda_{\text{exc}} = 532 \text{ nm}$) measured on liquid drops of the dispersions after the centrifugation steps as indicated in A) showing the increase in relative PL intensity related to the ML enrichment. C) UV-Vis extinction spectra normalized to 290 nm. Changes in the spectra region 200-250 nm are related to changes in length. Inset: A-exciton. Changes in the shape of the A-exciton are related to varying distributions of ML and FL WS_2 . D) Second derivatives of the A-exciton obtained after smoothing the spectrum with the Lowess method (10-15 points). The spectra were fitted to the second derivative of two Lorentzians as described in SI section 5.

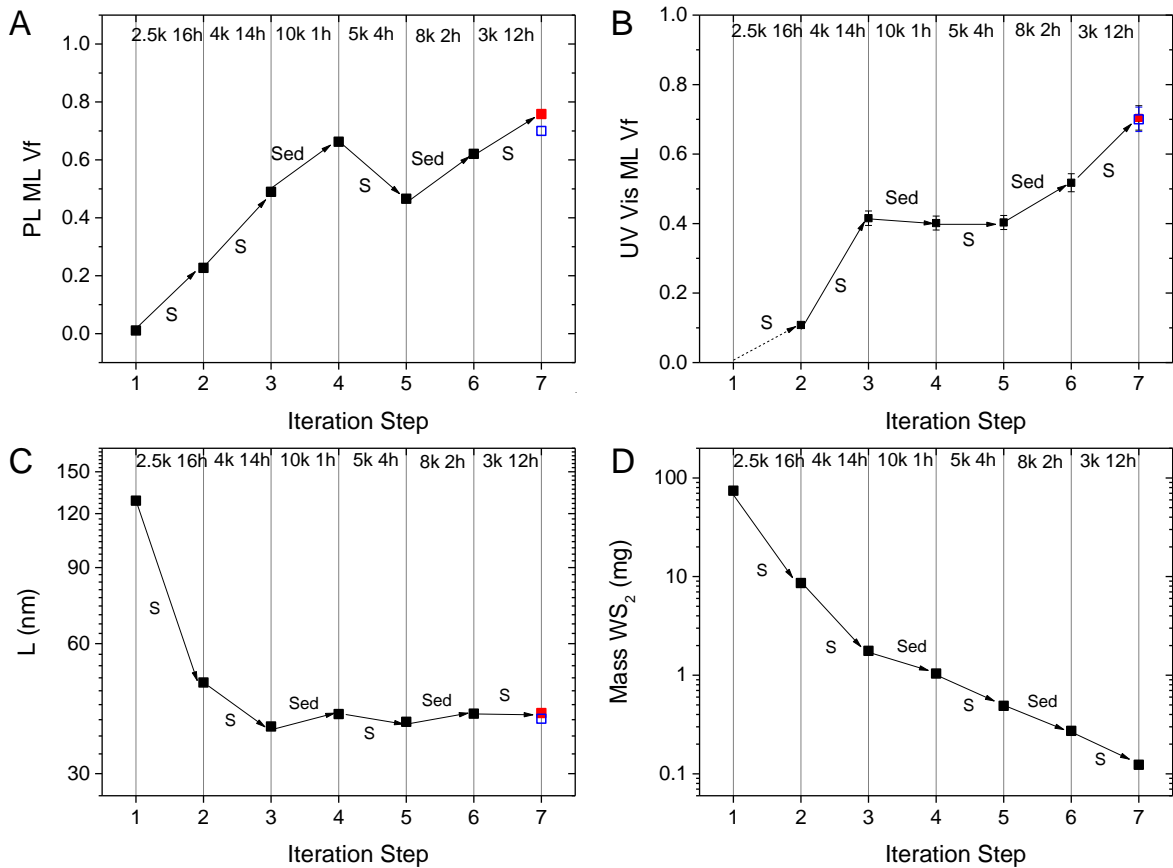


Figure S30: Summary of example 2 of the ML enrichment centrifugation procedure. The rotational speeds and times are indicated at the top of the individual panels. Blue data points indicate the samples that were subjected to AFM. The red data points are the result of the AFM analysis (see Figure S31). A) Volume fraction of monolayers determined from the PL/Raman metric of the supernatants (S) or sediments (Sed) after each iteration step. B) Volume fraction of monolayers determined from the UV-Vis A-exciton shape metric. Again, a strong discrepancy is observed when very small nanosheets are enriched. C) Mean length determined from the empirical UV-Vis peak intensity ratio Ext_{235}/Ext_{290} of the supernatants (S) or sediments (Sed) after each iteration step according to equation 3. The (corrected) length from AFM agrees very well with the metric data. D) Mass of WS_2 after each iteration step.

AFM on selected sample

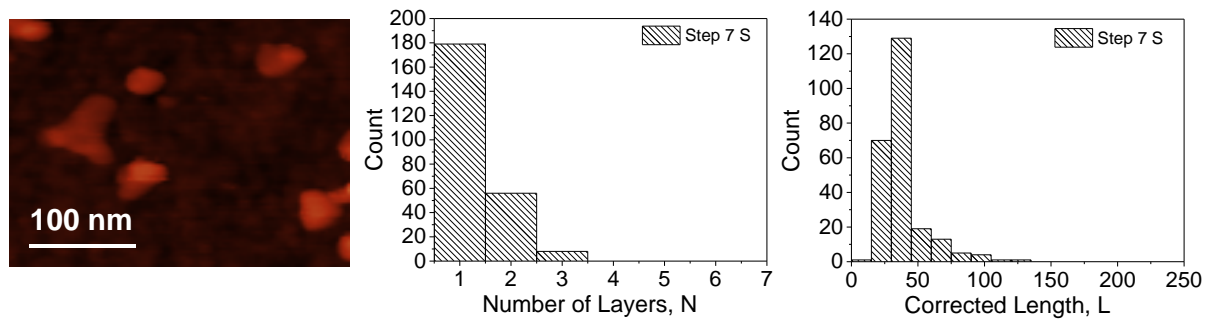


Figure S31: AFM analysis of selected samples of the monolayer enrichment procedure schematically shown in Figure S29A. Left: Representative images, middle panel: number of layer histograms. Right: Histograms of the (corrected) length.

6.4 Further optical characterization of ML-rich samples and edge effects

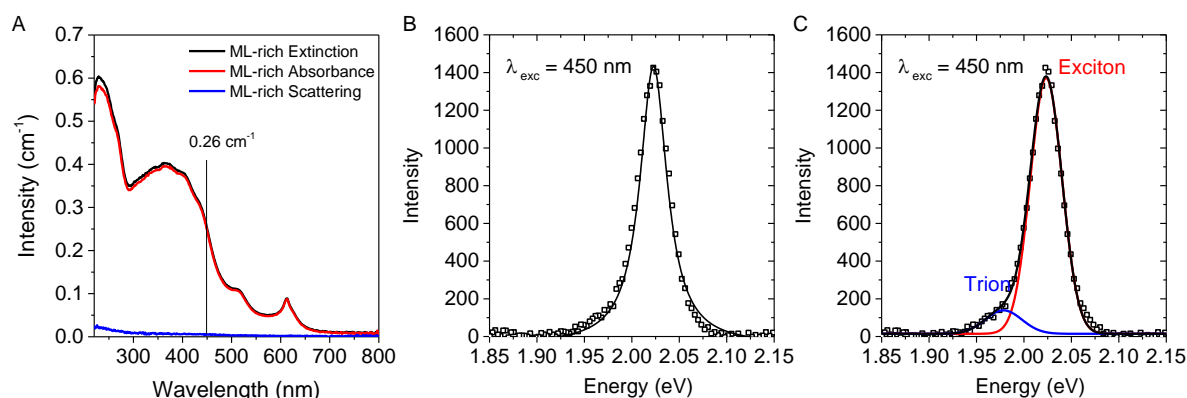


Figure S32: Extinction/Absorbance of the ML-rich dispersion. A) To confirm that scattering is negligible in the ML-rich sample (sediment after step 5 of the enrichment scenario 1) so that extinction is virtually identical to the absorbance, the sample was measured using an integrating sphere as described in Figure S11. The resultant absorbance is compared to the extinction spectrum in Figure S32A. The optical density at the excitation wavelength of the emission spectrum in Figure 6H of the main manuscript is indicated. B and C) Emission spectrum of the ML rich sample after excitation at 450 nm (measured in the PL spectrometer at the optical density indicated in A) fit to B) a single Lorentzian and C) two Gaussians. In contrast to the spectra recorded in the Raman spectrometer with an excitation wavelength of 532 nm (compare Figure S15), the PL spectrum can be fit well to two Gaussians if taking into account potential trion emission at lower energy. However, since the trion emission is small, spectra can still be fitted consistently well with one Lorentzians (see Figure S32B). For the sake of consistency and comparability, we have therefore used Lorentzian functions throughout this manuscript.

ML-rich samples: Impact of lateral size on photoluminescence

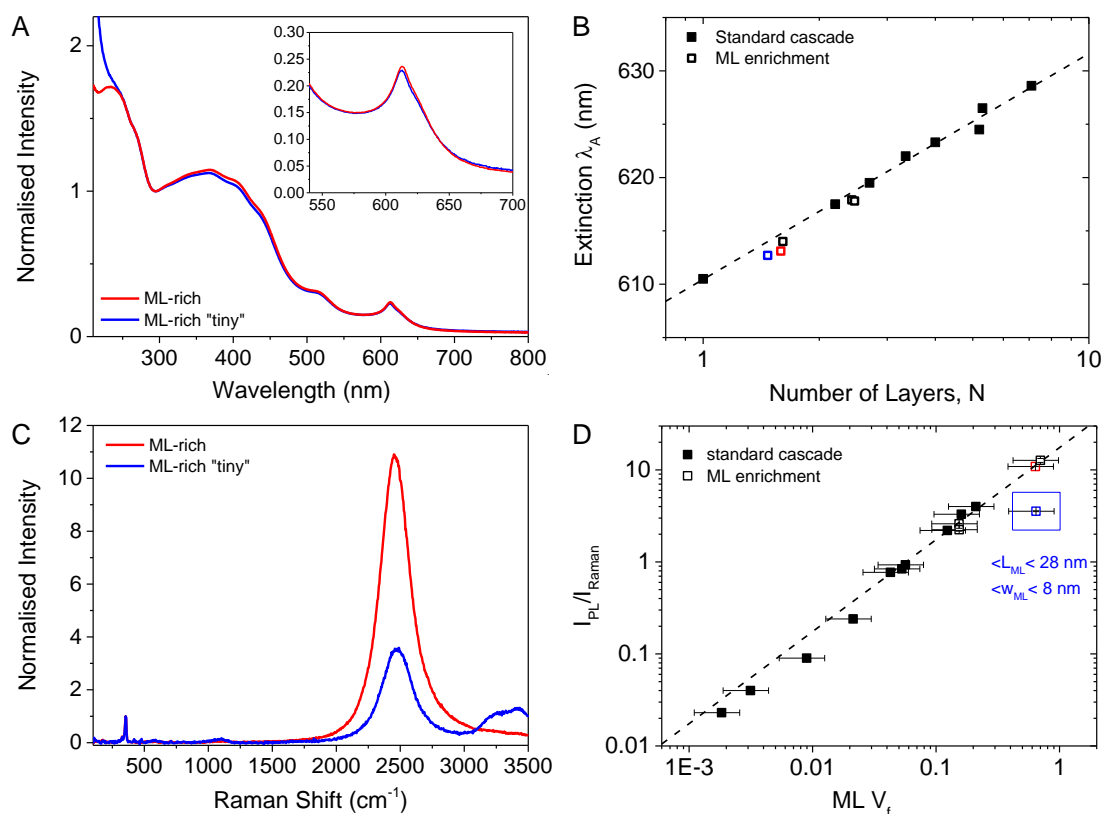


Figure S33: Edge effects on optical properties: comparison of monolayer-rich samples.

The sample denoted as ML-rich “tiny” is the supernatant after step 4 in the ML enrichment procedure 1, while the sample denoted as ML-rich is the sediment after step 5. The corresponding AFM images, N and L histograms are shown in Figure S28. In both cases, the volume fraction of ML according to AFM is $> 60\text{-}65\%$. A) Optical extinction spectra of the two samples. The differences in lateral size are reflected by changes in the spectral shape between 220 and 250 nm. Inset: A-exciton. The identical shape is consistent with similar volume fractions of MLs. B) Empirical relation of the A-exciton center of mass position *versus* mean thickness as shown in Figure 4D of the main manuscript with the samples from the ML enrichment included. They collapse on the same curve confirming that the determination of $\langle N \rangle$ is robust even for thinner nanosheets even though the 2nd derivatives need to be smoothed considerably more to determine the center of mass position. C) Raman/PL spectra of the two samples. Despite the similar ML volume fraction, the PL/Raman ratio of the dispersion containing very small nanosheets is significantly lower strongly suggesting PL quenching due to edge effects. D) Plot of PL/Raman intensity *versus* ML volume fractions with the sample from the ML enrichment included. The dispersion containing very small nanosheets (with a mean length of 28 nm and mean width [defined as the dimension perpendicular to length] of 8 nm) is a clear outlier.

We rationalize the reduced PL intensity in the dispersion containing very small WS₂ nanosheets by edge-activated trapping of excitons at defect sites such as edges.^{28, 29} The PL/Raman intensity will therefore not only depend on the volume fraction of monolayers, but also on the fraction of excitons that recombine radiatively from the basal plane. The latter can be expressed as fraction of the PL/Raman ratio over the volume fraction of monolayers. To test whether we can indeed observe trapping of excitons at edge states experimentally, we plot the fraction of the PL/Raman ratio over the volume fraction of monolayers as a function of the (AFM corrected) mean width of the WS₂ monolayers (w_{mono} corrected) in Figure S34A. We note that the nonradiative decay by edge states will be governed by the smallest dimension of the nanosheets. It is therefore more appropriate in this case to plot the data as a function of width rather than length.

We can assess this quantitatively by noting that we can write the PL/Raman ratio as

$$\frac{I_{PL}}{I_{Raman}} = \frac{(I_{PL} / V_{\text{mono}}) V_{\text{mono}}}{(I_{Raman} / V_{\text{all}}) V_{\text{all}}} \quad (\text{eq. S3})$$

Where V_{mono} and V_{all} are the total volume of all monolayers and all nanosheets respectively. Because $V_f = V_{\text{mono}} / V_{\text{all}}$, this means that

$$\frac{I_{PL} / I_{Raman}}{V_f} \propto \frac{I_{PL}}{V_{\text{mono}}} \quad (\text{eq. S4})$$

The right hand side is identical to the PL per monolayer divided by the volume per monolayer. For small monolayers with length, L , width, W , $L/W=k$, and edge thickness x (where all excitons are quenched), PL can only come from the central region (no more than x from the edge) so:

$$\begin{aligned} \frac{I_{PL} / I_{Raman}}{V_f} &\propto \frac{(L-2x)(W-2x)}{LW} = \frac{(kW-2x)(W-2x)}{kWW} = \\ &\frac{kWW - 2Wx(1+k) + 4xx}{kWW} = 1 - \frac{2x(1+k)}{kW} + \frac{4}{k} \left(\frac{x}{W} \right)^2 \end{aligned} \quad (\text{eq. S5})$$

This data fits reasonably well to the data taking $x=1.8$ nm ($k=1.65$).

The effect of edges on the optical properties is furthermore reflected in the PL line width as shown in Figure S34B. The PL width is plotted as a function of the mean ML area (approximated as nanosheet length \times width, an approximation that would be expected to

overestimate the area by a factor of 2^1) for both samples from the standard cascade and the ML enrichment cascade. It is evident that PL width increases for both the smallest nanosheets and the largest nanosheets. We suggest that the PL width, w_{PL} is proportional to the defect density which can be expressed as total number of defects N_D per area, A . N_D includes both edge and basal plane defects and is roughly related to the area *via*

$$N_D = k_1\sqrt{A} + k_2A \quad (\text{eq. S6})$$

where the edge length is proportional to the square root of A . However, it is possible that the basal plane defect density is not constant but depends on nanosheet size. To allow this, we write

$$N_D = k_1\sqrt{A} + k_2A^n \quad (\text{eq. S7})$$

where k_1 and k_2 are the number of basal plane and edge defects, respectively. In this simple model, the PL width is proportional to the area according to eq. S8.

$$w_{PL} \propto k_1A^{-0.5} + k_2A^{n-1} \quad (\text{eq. S8})$$

We have fitted this equation to the data in Figure S34, finding reasonable agreement for $n=1.25$. This implies that the basal plane defect density increases slightly with monolayer size.

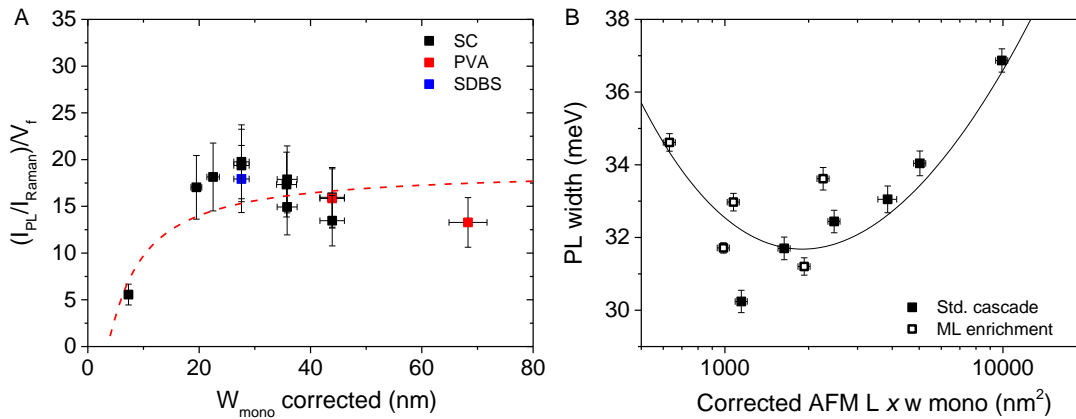


Figure S34: Manifestation of edge effects: A) Fraction of the PL/Raman intensity over ML volume fraction as a function of mean width of the WS_2 monolayers. Black data points are from WS_2 -SC dispersions, red data points from WS_2 -PVA and blue from WS_2 -SDBS. The red line is a fit to equation S5. The width of the edge region from the fit parameters is estimated

¹ A nanosheet with length, L , and width, w , can have a range of areas from $L \times w$ (rectangular) to approaching zero (cross-shaped). We expect the mean to be $\sim L \times w/2$.

to be 2 nm. B) PL linewidth, from Lorentzian fit, plotted *versus* lateral dimensions of the monolayer ($L \times w_{\text{mono}}$) for both samples obtained after size-selection using the standard cascade and the selected dispersions of the ML enrichment cascade. Edge effects are also reflected in the PL width which broadens as nanosheets become very small. The dashed line is a fit to eq. S8.

6.5 Example scenario 3

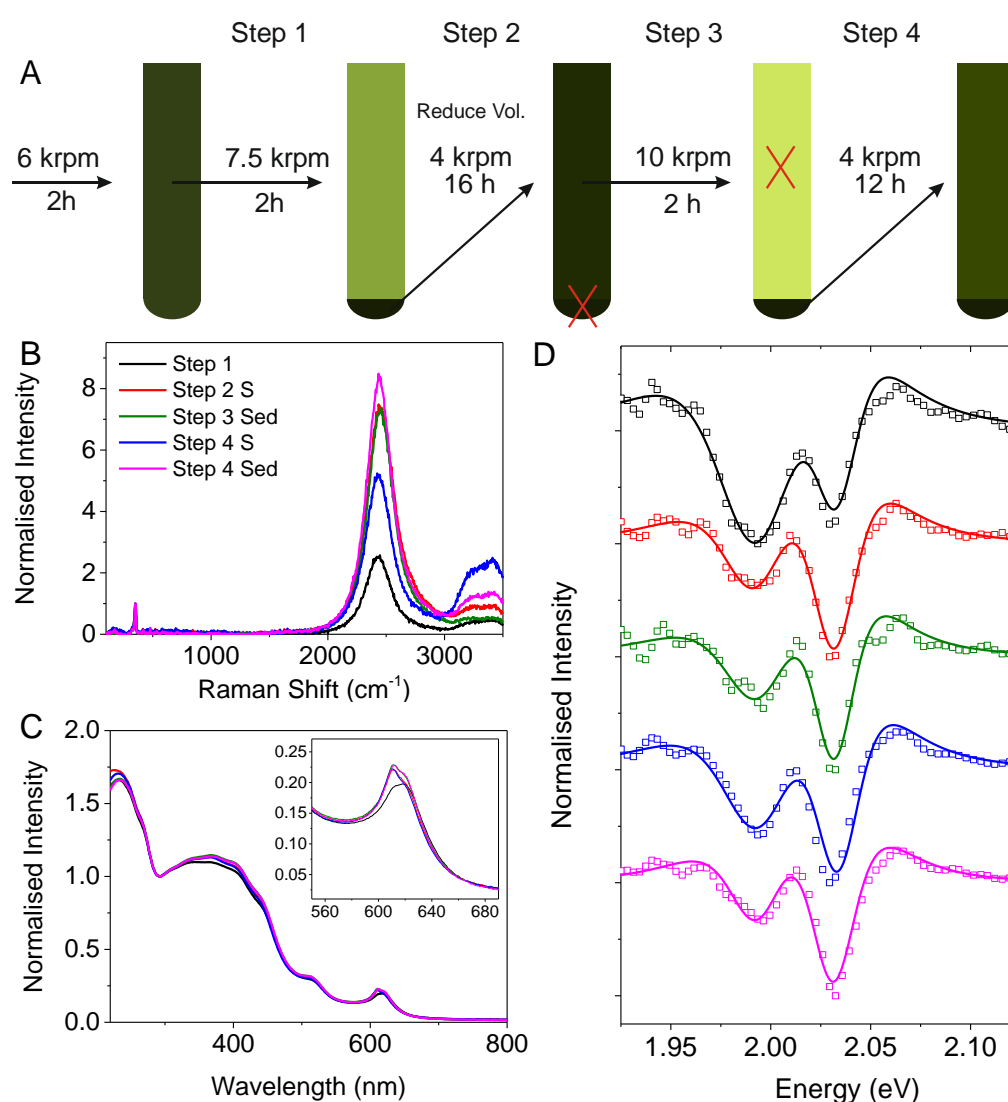


Figure S35: Spectroscopic data of example 3 of the monolayer enrichment. A) Schematic of the centrifugation procedure. B) Normalized Raman/PL spectra ($\lambda_{\text{exc}}= 532 \text{ nm}$) measured on liquid drops of the dispersions after the centrifugation steps as indicated in A). C) UV-Vis extinction spectra normalized to 290 nm. Inset: A-exciton. D) Second derivatives of the A-

exciton obtained after smoothing the spectrum with the Lowess method (10-15 points). The spectra were fitted to the second derivative of two Lorentzians as described in SI section 5.

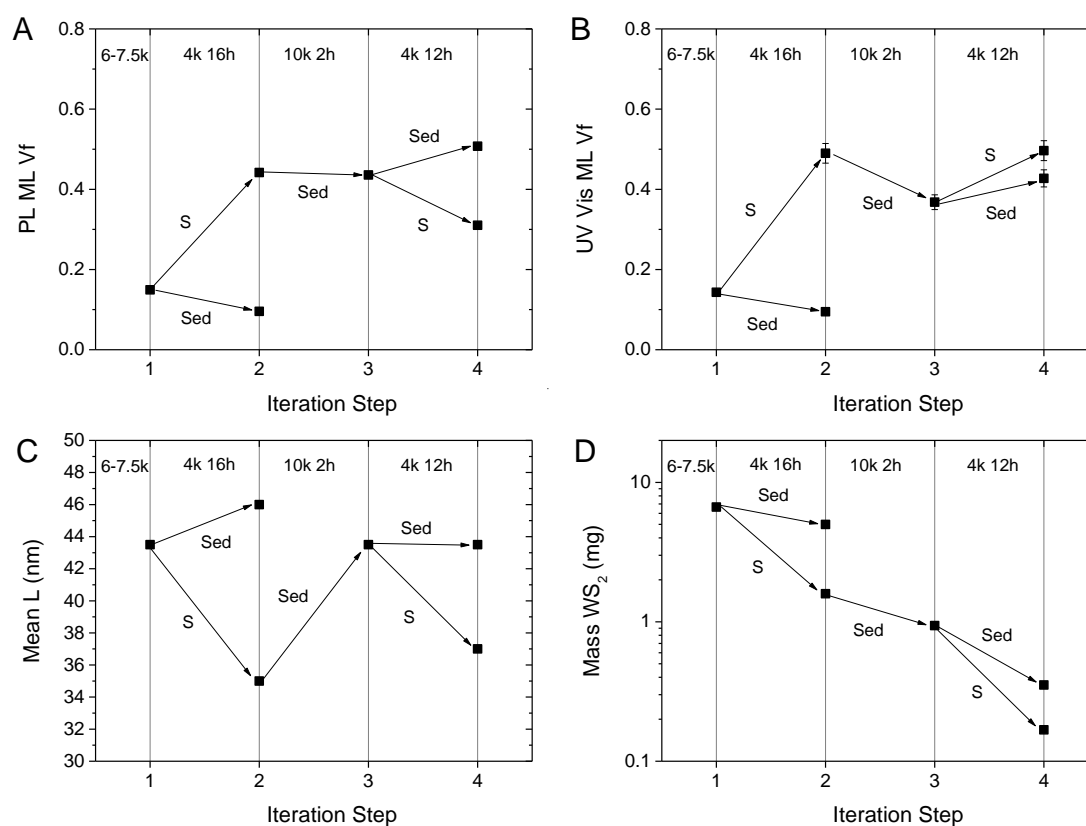


Figure S36: Summary of example 3 of the ML enrichment centrifugation procedure. The rotational speeds and times are indicated at the top of the individual panels. A) Volume fraction of monolayers determined from the PL/Raman metric of the supernatants (S) or sediments (Sed) after each iteration step. The supernatant after step 4 has a lower PL/Raman ratio (and hence apparent ML volume fraction) than the sediment due to PL quenching from edges. B) Volume fraction of monolayers determined from the UV-Vis A-exciton shape metric of the supernatants (S) or sediments (Sed) after each iteration step. C) Mean length determined from the empirical UV-Vis peak intensity ratio Ext_{235}/Ext_{290} of the supernatants (S) or sediments (Sed) after each iteration step according to equation 3 in the main manuscript. D) Mass of WS₂ after each iteration step.

6.6 Example Scenario 4

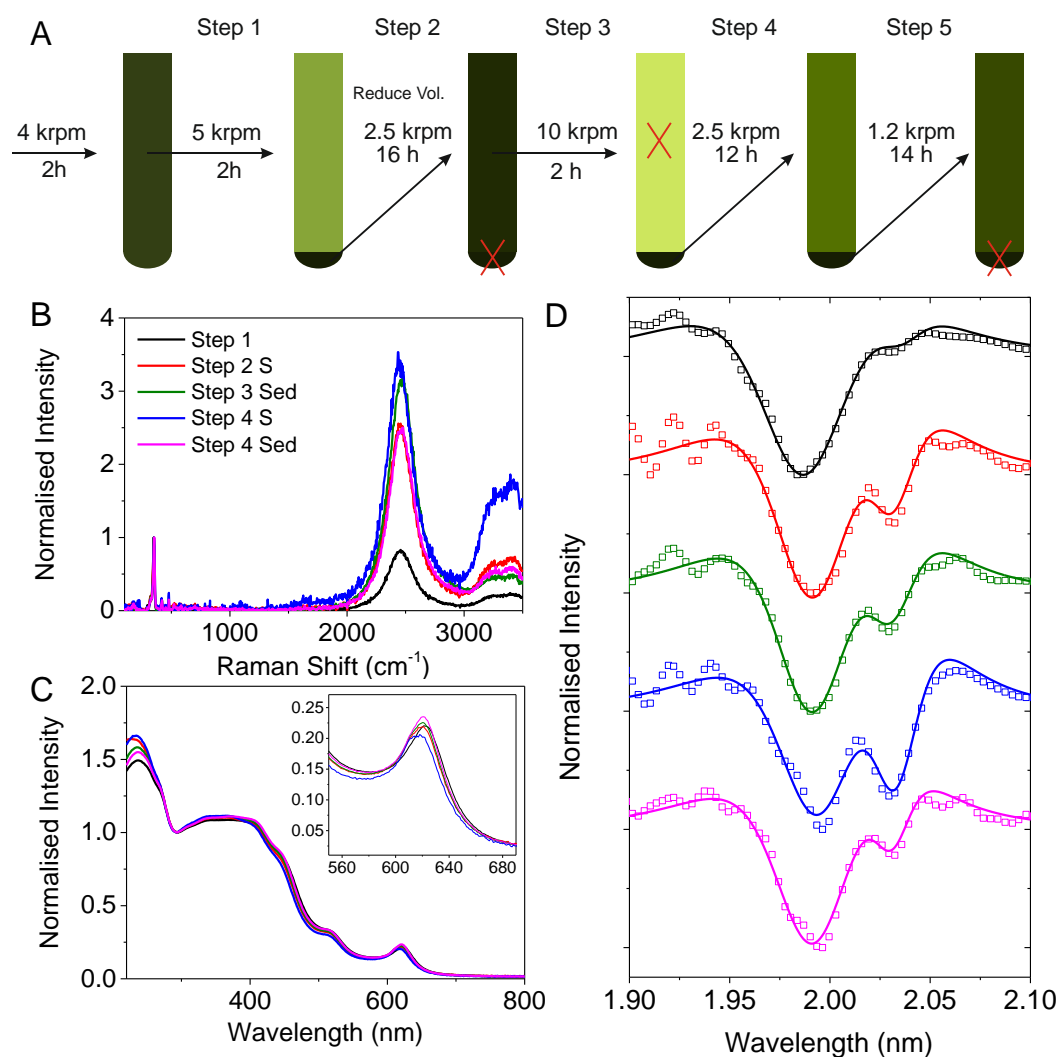


Figure S37: Spectroscopic data of example 4 of the monolayer enrichment. A dispersion containing larger/thicker nanosheets in mean was used as starting point (centrifuged between 4-5 krpm). A) Schematic of the centrifugation procedure. B) Normalized Raman/PL spectra ($\lambda_{\text{exc}} = 532 \text{ nm}$) measured on liquid drops of the dispersions after the centrifugation steps as indicated in A). C) UV-Vis extinction spectra normalized to 290 nm. Inset: A-exciton. D) Second derivatives of the A-exciton obtained after smoothing the spectrum with the Lowess method (10-15 points). The spectra were fitted to the second derivative of two Lorentzians as described in SI section 5.

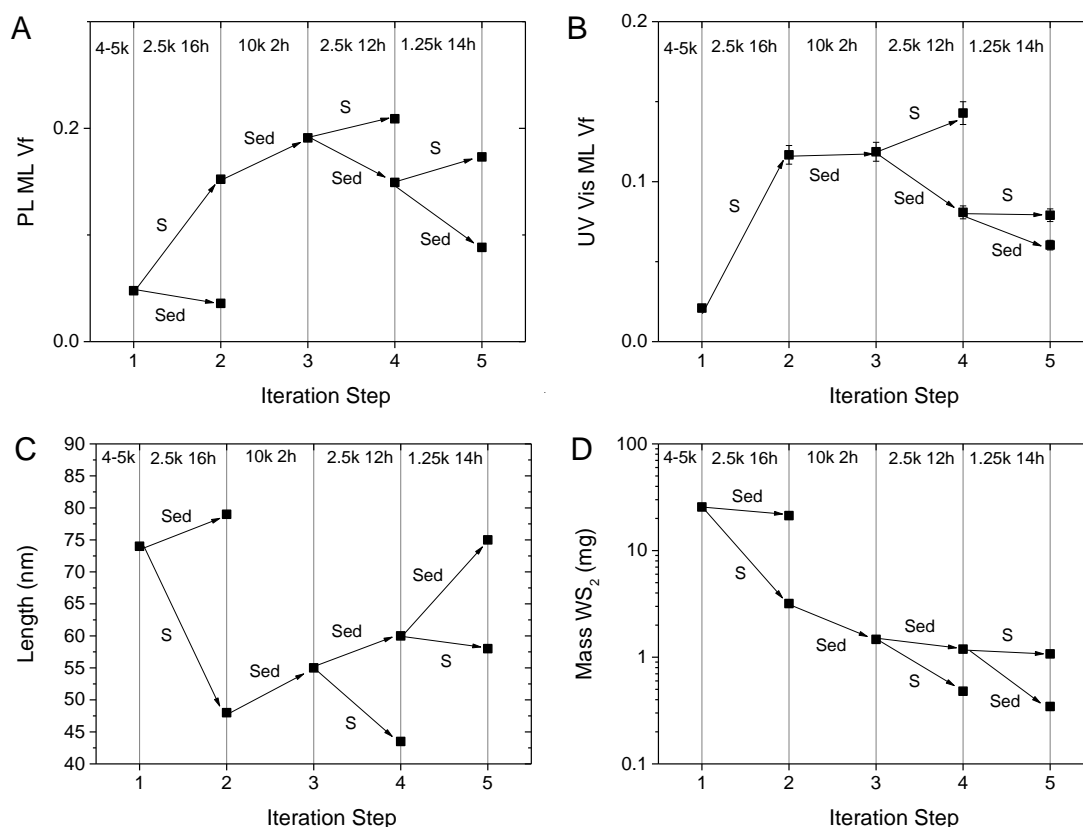


Figure S38: Summary of example 4 of the ML enrichment centrifugation procedure. The rotational speeds and times are indicated at the top of the individual panels. A) Volume fraction of monolayers determined from the PL/Raman metric of the supernatants (S) or sediments (Sed) after each iteration step. B) Volume fraction of monolayers determined from the UV-Vis A-exciton shape metric of the supernatants (S) or sediments (Sed) after each iteration step. Fits to two components in the second derivative of the A-exciton are challenging due to the lower ML V_f . In such cases, the PL/Raman metric is more reliable C) Mean length determined from the empirical UV-Vis peak intensity ratio Ext_{235}/Ext_{290} of the supernatants (S) or sediments (Sed) after each iteration step according to equation 3. D) Mass of WS_2 after each iteration step.

7 Fitting of the second derivatives of the A-exciton: methodology and examples of standard size-selected samples

In order to be able to deconvolute the extinction (absorbance) A-exciton peak into components of monolayered and few-layered WS₂, the spectra were smoothed by the Lowess method (10-15 points) prior to differentiation. This smoothing function is particularly suitable, as it suppresses spectral noise well without changing peak shapes. The as-obtained spectrum of the second derivative is then fitted to the sum of the second derivative of two Lorentzian functions. We note that to determine the center of mass peak position to determine mean N, the spectra are first differentiated and then smoothed with the Adjacent Averaging method.

A Lorentzian can be written as

$$L = \frac{h}{\left[1 + \left(\frac{(E - E_0)}{w/2} \right)^2 \right]} \quad (\text{eq. S9})$$

Where h is the height, E₀ is the centre and w is the FWHM. Differentiating twice with respect to E gives

$$\frac{d^2L}{dE^2} = -\frac{8h}{w^2} \left[\frac{1 - 3 \left(\frac{E - E_0}{w/2} \right)^2}{\left(1 + \left(\frac{E - E_0}{w/2} \right)^2 \right)^3} \right] \quad (\text{eq. S10})$$

The second derivative spectra were fitted to the sum of two second derivatives giving energy, width and height of the monolayer and few-layer WS₂. The fits to the samples from the standard size selection cascade are shown in Figure S39.

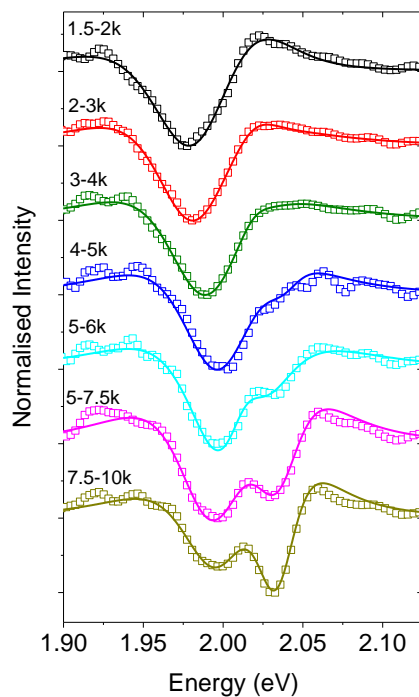


Figure S39: Second derivatives of the A-exciton of the samples after standard size selection obtained after smoothing the spectrum with the Lowess method (10-15 points). The spectra were fit to the second derivative of two Lorentzians as described above.

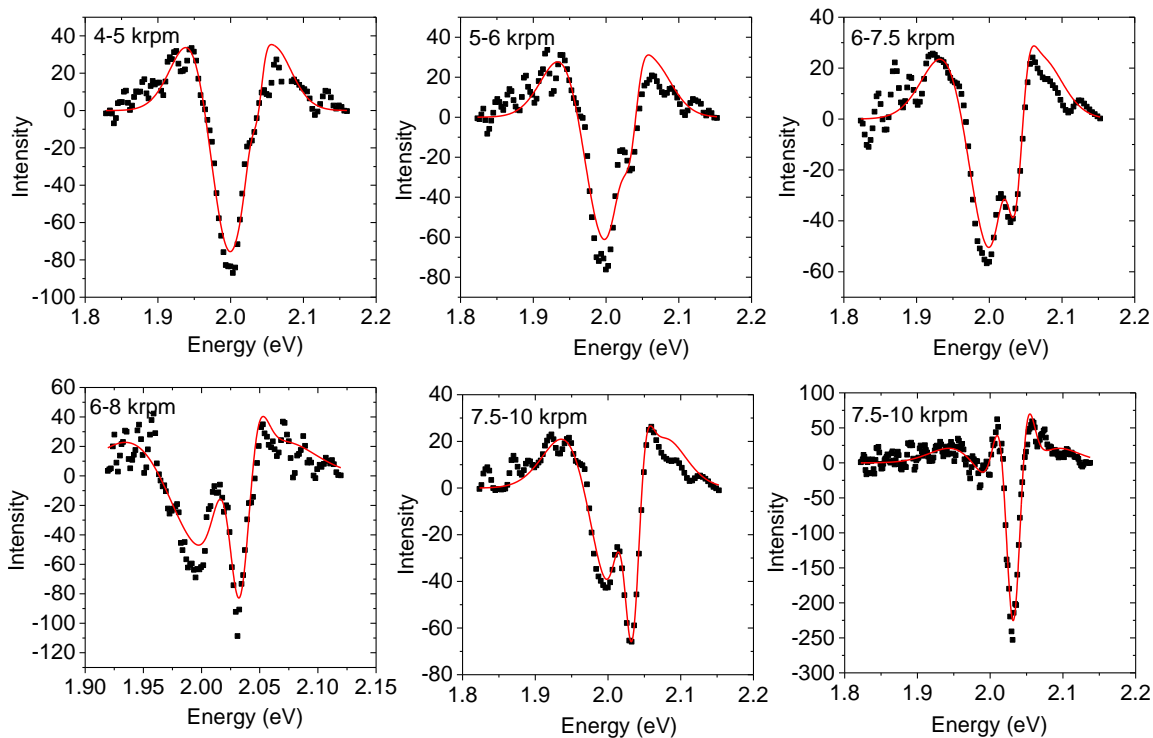


Figure S40: Examples of A-exciton second derivatives fitted to the second derivative of two Gaussians. The sample is indicated in the figure legend. While the fits are mostly reasonable, they are consistently worse than fits to the sum of two Lorentzians (compare Figure S38).

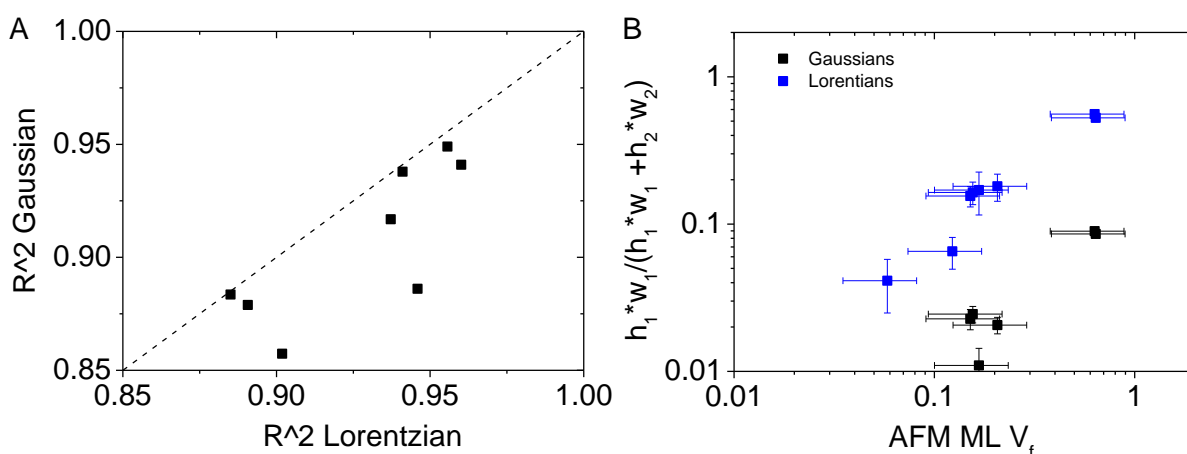


Figure S41: Lorentzian versus Gaussian fits of the absorbance A-exciton. A) The error in the fitting using Gaussians is higher compared to Lorentzians expressed as R^2 of the fits plotted versus each other. B) Most importantly, the monolayer V_f A-exciton shape metric cannot be applied when the A-exciton is fitted to second derivatives of Gaussians strongly

suggesting that the line shape is best described by Lorentzian functions even though an ensemble is probed.

8 Supporting References

1. Backes, C.; Smith, R. J.; McEvoy, N.; Berner, N. C.; McCloskey, D.; Nerl, H. C.; O'Neill, A.; King, P. J.; Higgins, T.; Hanlon, D.; Scheuschner, N.; Maultzsch, J.; Houben, L.; Duesberg, G. S.; Donegan, J. F.; Nicolosi, V.; Coleman, J. N., Edge and Confinement Effects Allow in Situ Measurement of Size and Thickness of Liquid-Exfoliated Nanosheets. *Nature Commun.* **2014**, *5*, 4576.
2. Yuan, S.; De Raedt, H.; Katsnelson, M. I., Modeling Electronic Structure and Transport Properties of Graphene with Resonant Scattering Centers. *Phys. Rev. B* **2010**, *82*, 115448.
3. Yuan, S.; Roldán, R.; De Raedt, H.; Katsnelson, M. I., Optical Conductivity of Disordered Graphene Beyond the Dirac Cone Approximation. *Phys. Rev. B* **2011**, *84*, 195418.
4. Roldán, R.; López-Sancho, M. P.; Guinea, F.; Cappelluti, E.; Silva-Guillén, J. A.; Ordejón, P., Momentum Dependence of Spin–Orbit Interaction Effects in Single-Layer and Multi-Layer Transition Metal Dichalcogenides. *2D Materials* **2014**, *1*, 034003.
5. Perdew, J. P.; Burke, K.; Ernzerhof, M., Generalized Gradient Approximation Made Simple. *Phys. Rev. Lett.* **1996**, *77*, 3865-3868.
6. Giannozzi, P.; Baroni, S.; Bonini, N.; Calandra, M.; Car, R.; Cavazzoni, C.; Ceresoli, D.; Chiarotti, G. L.; Cococcioni, M.; Dabo, I.; Dal Corso, A.; de Gironcoli, S.; Fabris, S.; Fratesi, G.; Gebauer, R.; Gerstmann, U.; Gougoussis, C.; Kokalj, A.; Lazzeri, M.; Martin-Samos, L., *et al.*, Quantum Espresso: A Modular and Open-Source Software Project for Quantum Simulations of Materials. *Journal of Physics-Condensed Matter* **2009**, *21*, 395502.
7. Kresse, G.; Furthmüller, J., Efficient Iterative Schemes for Ab Initio Total-Energy Calculations Using a Plane-Wave Basis Set. *Phys. Rev. B* **1996**, *54*, 11169-11186.
8. Kresse, G.; Hafner, J., Ab-Initio Molecular-Dynamics for Open-Shell Transition-Metals. *Phys. Rev. B* **1993**, *48*, 13115-13118.
9. Troullier, N.; Martins, J. L., Efficient Pseudopotentials for Plane-Wave Calculations. *Phys. Rev. B* **1991**, *43*, 1993-2006.
10. Blochl, P. E., Projector Augmented-Wave Method. *Phys. Rev. B* **1994**, *50*, 17953-17979.
11. Kresse, G.; Joubert, D., From Ultrasoft Pseudopotentials to the Projector Augmented-Wave Method. *Phys. Rev. B* **1999**, *59*, 1758-1775.
12. Marini, A.; Hogan, C.; Gruening, M.; Varsano, D., Yambo: An Ab Initio Tool for Excited State Calculations. *Comput. Phys. Commun.* **2009**, *180*, 1392-1403.
13. Monkhorst, H. J.; Pack, J. D., Special Points for Brillouin-Zone Integrations. *Phys. Rev. B* **1976**, *13*, 5188-5192.
14. Paton, K. R.; Varrla, E.; Backes, C.; Smith, R. J.; Khan, U.; O'Neill, A.; Boland, C.; Lotya, M.; Istrate, O. M.; King, P.; Higgins, T.; Barwich, S.; May, P.; Puczkarski, P.; Ahmed, I.; Moebius, M.; Pettersson, H.; Long, E.; Coelho, J.; O'Brien, S. E., *et al.*, Scalable Production of Large Quantities of Defect-Free Few-Layer Graphene by Shear Exfoliation in Liquids. *Nat. Mater.* **2014**, *13*, 624-630.
15. Eda, G.; Yamaguchi, H.; Voiry, D.; Fujita, T.; Chen, M.; Chhowalla, M., Photoluminescence from Chemically Exfoliated Mos₂. *Nano Lett.* **2011**, *11*, 5111-5116.
16. Harvey, A.; Backes, C.; Gholamvand, Z.; Hanlon, D.; McAteer, D.; Nerl, H. C.; McGuire, E.; Seral-Ascaso, A.; Ramasse, Q. M.; McEvoy, N.; Winters, S.; Berner, N. C.; McCloskey, D.; Donegan, J.; Duesberg, G.; Nicolosi, V.; Coleman, J. N., Preparation of Gallium Sulfide Nanosheets by Liquid Exfoliation and Their Application as Hydrogen Evolution Catalysts. *Chem. Mater.* **2015**, *27*, 3483-3493.
17. Hanlon, D.; Backes, C.; Doherty, E.; Cucinotta, C. S.; Berner, N. C.; Boland, C.; Lee, K.; Lynch, P.; Gholamvand, Z.; Harvey, A.; Zhang, S.; Wang, K.; Moynihan, G.; Pokle, A.; Ramasse, Q. M.; McEvoy, N.; Blau, W. J.; Wang, J.; Abellan, G.; Hauke, F., *et al.*, Liquid Exfoliation of Solvent-Stabilised Few-Layer Black Phosphorus for Applications Beyond Electronics. *Nature Commun.* **2015**, *6*, 8563.
18. Ridings, C.; Warr, G. G.; Andersson, G. G., Composition of the Outermost Layer and Concentration Depth Profiles of Ammonium Nitrate Ionic Liquid Surfaces. *Phys. Chem. Chem. Phys.* **2012**, *14*, 16088-16095.

19. Nemes-Incze, P.; Osváth, Z.; Kamarás, K.; Biró, L. P., Anomalies in Thickness Measurements of Graphene and Few Layer Graphite Crystals by Tapping Mode Atomic Force Microscopy. *Carbon* **2008**, *46*, 1435-1442.
20. Nacken, T. J.; Damm, C.; Walter, J.; Ruger, A.; Peukert, W., Delamination of Graphite in a High Pressure Homogenizer. *RSC Adv.* **2015**, *5*, 57328-57338.
21. Yadgarov, L.; Choi, C. L.; Sedova, A.; Cohen, A.; Rosentsveig, R.; Bar-Elli, O.; Oron, D.; Dai, H.; Tenne, R., Dependence of the Absorption and Optical Surface Plasmon Scattering of Mos₂ Nanoparticles on Aspect Ratio, Size, and Media. *ACS Nano* **2014**, *8*, 3575-3583.
22. Peimyoo, N.; Yang, W.; Shang, J.; Shen, X.; Wang, Y.; Yu, T., Chemically Driven Tunable Light Emission of Charged and Neutral Excitons in Monolayer Ws₂. *ACS Nano* **2014**, *8*, 11320-11329.
23. Lin, Y.; Ling, X.; Yu, L.; Huang, S.; Hsu, A. L.; Lee, Y.-H.; Kong, J.; Dresselhaus, M. S.; Palacios, T., Dielectric Screening of Excitons and Trions in Single-Layer Mos₂. *Nano Lett.* **2014**, *14*, 5569-5576.
24. Mak, K. F.; He, K.; Lee, C.; Lee, G. H.; Hone, J.; Heinz, T. F.; Shan, J., Tightly Bound Trions in Monolayer Mos₂. *Nat. Mater.* **2013**, *12*, 207-211.
25. Gutiérrez, H. R.; Perea-López, N.; Elías, A. L.; Berkdemir, A.; Wang, B.; Lv, R.; López-Urías, F.; Crespi, V. H.; Terrones, H.; Terrones, M., Extraordinary Room-Temperature Photoluminescence in Triangular Ws₂ Monolayers. *Nano Lett.* **2012**, *13*, 3447-3454.
26. Zhao, W.; Ghorannevis, Z.; Chu, L.; Toh, M.; Kloc, C.; Tan, P.-H.; Eda, G., Evolution of Electronic Structure in Atomically Thin Sheets of Ws₂ and Wse₂. *ACS Nano* **2012**, *7*, 791-797.
27. Kobayashi, Y.; Sasaki, S.; Mori, S.; Hibino, H.; Liu, Z.; Watanabe, K.; Taniguchi, T.; Suenaga, K.; Maniwa, Y.; Miyata, Y., Growth and Optical Properties of High-Quality Monolayer Ws₂ on Graphite. *ACS Nano* **2015**, *9*, 4056-4063.
28. Shi, H.; Yan, R.; Bertolazzi, S.; Brivio, J.; Gao, B.; Kis, A.; Jena, D.; Xing, H. G.; Huang, L., Exciton Dynamics in Suspended Monolayer and Few-Layer Mos₂ 2d Crystals. *ACS Nano* **2013**, *7*, 1072-1080.
29. Huang, J. M.; Laitinen, R. A.; Kelley, D. F., Spectroscopy and Trapping Dynamics in Ws₂ Nanoclusters. *Phys. Rev. B* **2000**, *62*, 10995-11005.